Complexity of resting brain dynamics shaped by multiscale structural constraints

— **Source link** ↗

Mengsen Zhang, Manish Saggar

Institutions: Stanford University

Related papers:

- Mapping the dynamic repertoire of the resting brain

- Neural network spectral robustness under perturbations of the underlying graph

- Putting the "dynamic" back into dynamic functional connectivity

- Binary mesoscale architecture does not explain controllability of structural brain networks

- Synchronization in Functional Networks of the Human Brain

Complexity of intrinsic brain dynamics shaped by multiscale structural constraints

Mengsen Zhang* and Manish Saggar*

Department of Psychiatry and Behavior Sciences,
Stanford University, Stanford, CA 94304

* Correspondence: mengsenz@stanford.edu, saggar@stanford.edu

Abstract

The brain is a complex, nonlinear system, exhibiting ever-evolving patterns of activities even without external inputs or tasks. Such intrinsic dynamics play a key role in cognitive functions and psychiatric disorders. A challenge is to link the intrinsic dynamics to the underlying structure, given the nonlinearity. Here we use a biophysically constrained, nonlinear-dynamical model to show how the complexity of intrinsic brain dynamics, manifested as its multistability and temporal diversity, can be sculpted by structural properties across scales. At a local level, multistability and temporal diversity can be induced by sufficient recurrent excitatory connectivity and its heterogeneity. At a global level, such functional complexity can also be created by the synergistic interaction between monostable, locally identical regions. Coordination between model brain regions across attractors in the multistable landscape predicts human functional connectivity. Compared to dynamics near a single attractor, cross-attractor coordination better accounts for functional links uncorrelated with structural connectivity. Energy costs of cross-attractor coordination are modulated by both local and global connectivity, and higher in the Default Mode Network. These findings hint that functional connectivity underscores transitions between alternative patterns of activity in the brain—even more than the patterns themselves. This work provides a systematic framework for characterizing intrinsic brain dynamics as a web of cross-attractor transitions and their energy costs. The framework may be used to predict transitions and energy costs associated with experimental or clinical interventions.

Significance Statement

The brain is a multifunctional system: different brain regions can coordinate flexibly to perform different tasks. Understanding the regional and global structural constraints on brain function is critical to understand cognition. Here, using a unified biophysical network model, we show how structural constraints across scales jointly shape the brain's intrinsic functional repertoire – the set of all possible patterns that a brain could generate. The modeled functional repertoire is enriched by both the flexibility of individual brain regions and their synergistic interaction in a global network. By carefully examining the modeled repertoire, we found that human resting-state functional connectivity was better predicted by transitions between brain activity patterns rather than any specific pattern per se.

1

1   Introduction

A fundamental goal of neuroscience is to understand how the structure of the brain constrains its function [1]. The brain's multiscale and nonlinear nature makes it challenging [2–4]. Relevant structural factors are scattered across scales, while nonlinearity makes it difficult to predict dynamic properties of the whole from its parts. Nonlinear dynamical models serve as essential tools for bridging structural and functional understanding of the brain [5, 6]. When equipped with plausible biophysical and connectivity features of the brain, biophysical network models have successfully provided insights into resting brain dynamics (e.g. [7–9]). However, their dynamic capability has not been extensively studied or fully utilized with regard to key nonlinear features such as multistability (c.f. [10]) and rhythmic activities. Here we first provide a systematic analysis of how the dynamic landscape of the model brain, its multistability and temporal diversity, vary with structural properties across scales. Further, we show that functional connectivity patterns as observed in human resting-state fMRI emerge spontaneously from the multistable landscape, reflecting the coordination between brain regions *across* attractors in the dynamic landscape.

Intrinsic brain dynamics have long been observed [11, 12], but often treated as a baseline subtracted from task-positive activities. This baseline, however, is more active than meets the eye: it consumes the largest fraction of the brain's energy resources, while task-related consumption adds little [13]. It constrains task performance and related neural activities across multiple time scales [14–16], and sustains alteration in neurological and psychiatric disorders [17]. Neuroimaging studies reveal the richness of such intrinsic brain dynamics and its subnetworks [18–24]. These empirical findings drive the development of large-scale models of resting brain dynamics (see [25] for a review), to reveal its functional purpose [5, 26] and as tools for mechanistic diagnostics of psychiatric disorders [27].

Nonlinear dynamical systems are often chosen over linear ones to account for the ubiquitous multistability and coordinated rhythmic activities in biological systems—the brain is one of the best examples [28–32]. To say that a system is multistable is to say that multiple stable patterns of activities (attractors) are all achievable by the system. Which pattern is retrieved depends on the external input or intrinsic noise. Multistability of the brain signifies its multi-functionality and its ability to form memory as persistent patterns of activity [2, 28, 33, 34]. The switching dynamics between functional networks in the resting brain is thought to reflect noise-driven exploration of the underlying multistable landscape, i.e. the brain's intrinsic functional repertoire [35]. On the other hand, brain dynamics is parsed in time by a hierarchy of diverse rhythmic activities [32, 36, 37]. The coordination across rhythmic activities at diverse frequencies gives rise to dynamic and flexible integration-segregation across multiple scales [32, 38]. Disruption of such temporal coordination is associated with neuropsychiatric disorders [39]. Together, multistability and temporal diversity are key features of intrinsic neural dynamics that theorists seek to capture using large-scale nonlinear dynamical models [10, 40, 41].

In the present work, we use a nonlinear dynamical model that incorporates structural properties of the brain across scales—from neurons, to local populations, and to large-scale networks. The model is a formal unification of the Wilson-Cowan model [42, 43] and the reduced Wong-Wang model [7, 8, 44]. The Wilson-Cowan model [42, 43] is a population-level model of brain dynamics, widely used for modeling multistability and rhythmic activity in large-scale brain networks [40, 45–50]. It is unconstrained by the biophysical properties of underlying neurons that may be important for predicting the outcome of electrical or pharmacological stimulation in empirical settings (e.g. [51, 52]). The reduced Wong-Wang model is a biophysical network model constrained by biologically plausible parameters at the neuronal level [34, 53–57]. Its noise-driven dynamics near certain attractors has been used to capture resting-state functional connectivity (e.g. [8, 9]). However, its reduced nonlinearity limits the multistability and makes it less viable for studying oscillations.

2

Our unified model retains both the nonlinearity of the Wilson-Cowan model and the biophysical constraints of the reduced Wong-Wang model.

With this model, we show how the intrinsic dynamic landscape of the brain can be shaped by structural properties across scales, and how multistability of the landscape gives rise to functional connectivity patterns and its energy demands.

2 Materials and Methods

2.1 The present model

Our model describes the whole-brain dynamics as the mean-field activity of neuronal populations in each brain region. Each model region contains a pair of excitatory (E) and inhibitory (I) populations, whose activity is described by the *local model* (Figure 1a, left box; equation 1-3) in terms of the state variables S_E and S_I. Physically, S_E and S_I are interpreted as the fraction of open synaptic channels in their respective populations, named the gating variables. Through local connections (w's), the excitatory population excites itself with strength w_{EE} and the inhibitory population with strength w_{EI}, while the inhibitory population inhibits itself with strength w_{II} and the excitatory population with strength w_{IE}. Local models further connect to each other through a global network (Figure 1a, dashed lines), i.e. the *global model* (right; equation 4-6). In the present work, nodes of the global network correspond to anatomical regions in the human brain based on a 66-region parcellation used in [7, 58] (Figure 1b); the weight of edges reflects the strength of long-range structural connectivity between brain regions, either estimated using structural data from the Human Connectome Project [59, 60] (Section 2.4.1) or artificial constructed for comparison.
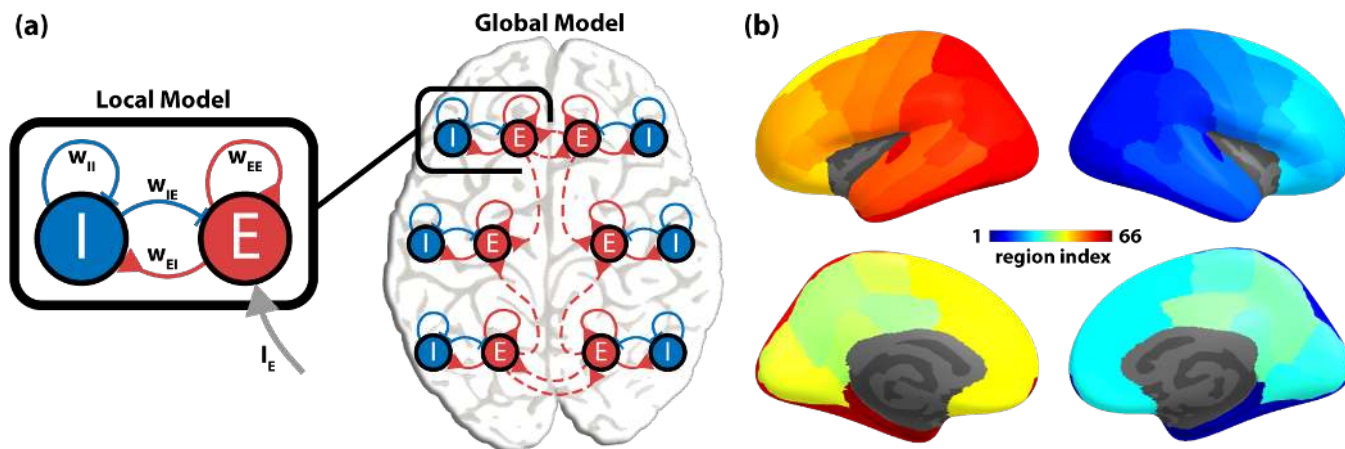

Figure 1: **Construction of a dynamic mean-field model of the human brain.** (a) The model brain (global model) consists of a network of brain regions (local model). The local model (black box) describes the interaction between two local neural populations — one excitatory E and one inhibitory I — via two excitatory connections (red, w_{EE} and w_{EI}) and two inhibitory connections (blue, w_{II} and w_{IE}). The excitatory population of each brain region can further receive input (gray arrow, I_E) from other regions, allowed by the large-scale structural connectivity (red dashed connections). (b) Nodes in the global model corresponds to 66 anatomical regions of the human brain, which can be linked together by the human connectome (see text). Regions are index from 1 to 66 (1-33 on the right hemisphere, 34-66 on the left hemisphere is reverse order, following [7]).

3

The local model is described by the equations,

$$\frac{\mathrm{d}\,S_E}{\mathrm{d}\,t} = -\frac{S_E}{\tau_E} + (1 - S_E)\gamma_E\,H_E(w_{EE}S_E - w_{IE}S_I + I_E) \tag{1}$$

$$\frac{\mathrm{d}\,S_I}{\mathrm{d}\,t} = -\frac{S_I}{\tau_I} + (1 - S_I)\gamma_I\,H_I(w_{EI}S_E - w_{II}S_I + I_I). \tag{2}$$

The activity of each population has a natural decay time of τ_E and τ_I respectively. Each population's activity tends to increase with the fraction of closed channels $(1 - S_p)$ and the population firing rate (H_p), scaled by a factor γ_p for $p \in \{E, I\}$. This is described by the second term on the right-hand-side of equation 1-2. H_E and H_I are transfer functions that map synaptic current input to population firing rate of the excitatory and the inhibitory population respectively (for example, H_E shown in Figure 2 as a black curve). In particular, they are sigmoidal functions of the form

$$H_p(x) = \frac{r_{max} + \dfrac{a_p x - b_p - r_{max}}{1 - e^{d_p(a_p x - b_p - r_{max})}}}{1 - e^{-d_p(a_p x - b_p)}}, \tag{3}$$

whose output increases with input monotonically and saturates at r_{max}—the maximal firing rate limited by the absolute refractory period of neurons (around 2 ms in certain cell types [61, 62]). The specific shape of each transfer function is determined by three additional parameters a_p, b_p and d_p (a_p and b_p determine the location and slope of the near-linear segment in the middle; d_p determines the smoothness of the corners bordering the said near-linear segment). This transfer function is converted from Wong and Wang's original formulation [44, 63] (a soft rectifier function, equation 13, orange dashed line in Figure 2) into a sigmoidal form (black solid line in Figure 2), while retaining the original value of parameters a_p, b_p, and d_p (shown in Table 1). The parameters were chosen to approximate the average response of a population of spiking pyramidal cells ($p = E$) and interneurons ($p = I$) respectively, incorporating physiologically plausible parameters [44, 57].
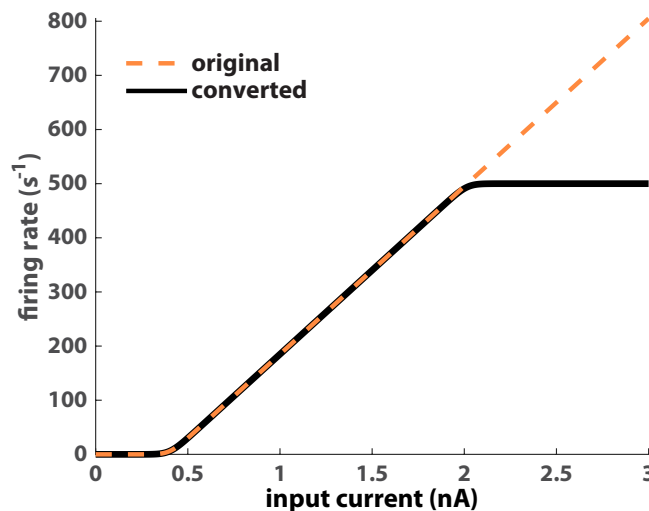

Figure 2: **Converting a rectifier transfer function to a sigmoidal form.** Black solid line is the transfer function used in the present model H_E (equation 3). It matches the transfer function used by Wong and Wang in their original formulation [44, 63] (orange dashed line; equation 13) for a low level of input. For a high level of input, $H_E(x)$ saturates at $r_{max} = 500$ (Hz), while the Wong-Wang's original version continues to scale (almost) linearly with input.

Interaction between local populations is modulated by four coupling parameters $w_{pq} \geqslant 0$ in equation 1-2, indicating the influence from the local population p to

4

q, where $p, q \in \{E, I\}$ (Figure 1 left box). These coupling parameters reflect the local structural connectivity. The local populations are also capable of responding to external current inputs denoted as I_E and I_I in equation 1-2, respectively. Importantly, such input can come from other brain regions in a globally connected network (Figure 1 right panel, dashed lines). This leads us to the global model. Formally, we substitute I_E in the local model (equation 1) with a global input I_G (equation 4),

$$\frac{\mathrm{d}\, S_E^{(i)}}{\mathrm{d}\, t} = -\frac{S_E^{(i)}}{\tau_E} + (1 - S_E^{(i)})\gamma_E H_E \left(w_{EE}^{(i)} S_E^{(i)} - w_{IE}^{(i)} S_I^{(i)} + I_G^{(i)}(\vec{S}_E) \right) + \sigma \xi_E^{(i)}(t) \quad (4)$$

$$\frac{\mathrm{d}\, S_I^{(i)}}{\mathrm{d}\, t} = -\frac{S_I^{(i)}}{\tau_I} + (1 - S_I^{(i)})\gamma_I H_I \left(w_{EI}^{(i)} S_E^{(i)} - w_{II}^{(i)} S_I^{(i)} + I_I \right) + \sigma \xi_I^{(i)}(t) \quad (5)$$

where $S_E^{(i)}$ and $S_I^{(i)}$ are the synaptic gating variable of the excitatory and the inhibitory population of the ith brain region respectively, and $\xi_\bullet^{(i)}$ is a noise term scaled to an amplitude σ. The state of all excitatory populations is denoted as a vector $\vec{S}_E$, the ith element of which is $S_E^{(i)}$. The global input to the ith brain region depends on both its connectivity with, and the ongoing state of, other brain regions,

$$I_G^{(i)}(\vec{S}_E) = G \sum_{\substack{j=1 \\ j \neq i}}^{N} C_{ij} S_E^{(j)} \quad (6)$$

where N denotes the total number of brain areas, $C_{ij} \geqslant 0$ the long-range structural connectivity from the jth to the ith brain region and G is a global coupling parameter that controls the overall level of interaction across brain regions. Since C_{ij} is only intended to represent long-range connectivity, we let $C_{ij} = 0$ for any $i = j$ to preclude recurrent connections. For the effects of G and C_{ij} to be independently comparable, here we impose a normalization condition on the matrix norm,

$$\|\mathbf{C}\|_\infty = \max_i \left(\sum_{j=1}^{N} |C_{ij}| \right) \equiv 1. \quad (7)$$

Since the global coupling parameter G modulates the level of input to each brain region, one would expect it to have comparable influence on the local dynamics as I_E in the local model (equation 1).

Next, we discuss its formal connection to two well-studied mean-field models of brain dynamics, namely, the Wilson-Cowan model (Section 2.2) [42, 43] and the reduced Wong-Wang model (Section 2.3) [8, 44].

5

parameter	interpretation	value
τ_E	decay time of NMDA receptor	0.1 (s)
τ_I	decay time of GABA receptor	0.01 (s)
γ_E	kinetic parameter of excitatory population	0.641
γ_I	kinetic parameter of inhibitory population	1
a_E	parameter of H_E	310 (nC^{-1})
b_E	parameter of H_E	125 (Hz)
d_E	parameter of H_E	0.16 (s)
a_I	parameter of H_I	615 (nC^{-1})
b_I	parameter of H_I	177 (Hz)
d_I	parameter of H_I	0.087 (s)
r_{max}	maximal firing rate	500 (Hz)
w_{EE}	excitatory-to-excitatory coupling	$\sim$ (nA)
w_{EI}	excitatory-to-inhibitory coupling	$\sim$ (nA)
w_{IE}	inhibitory-to-excitatory coupling	$\sim$ (nA)
w_{II}	inhibitory-to-inhibitory coupling	0.05 (nA)
I_E	external input to excitatory population	$\sim$ (nA)
I_I	external input to inhibitory population	0.1 (nA)
G	global coupling	$\sim$ (nA)
C_{ij}	structural connectivity between brain regions	$\sim$
σ	noise amplitude	$\sim$

Table 1: **The interpretation and value of model parameters.** Here we summarize the parameters used in equation 1-5. Most parameters assume a fixed value, which was introduced by [44]. A "$\sim$" indicates that this parameter is manipulated in the present study to explore the behavior of the model.

2.2 Relation to the Wilson-Cowan model

Formally, the above model can be considered a special variant of the Wilson-Cowan model [42, 43]. Though the specific interpretation of certain parameters differ, the two models describe similar dynamic mechanisms of population-level interaction. The Wilson-Cowan model, in its initial form [42], concerns the dynamics of a pair of interacting excitatory and inhibitory neuronal populations. The activities of the two populations are denoted as $E(t)$ and $I(t)$—the proportion of firing excitatory/inhibitory cells averaged over a period of time (the refectory period). The model takes the form

$$\tau_E \frac{d E}{d t} = -E + (k_E - r_E E)\mathscr{S}_E(c_1 E - c_2 I + P) \tag{8}$$

$$\tau_I \frac{d I}{d t} = -I + (k_I - r_I I)\mathscr{S}_I(c_3 E - c_4 I + Q). \tag{9}$$

τ_E and τ_I are time constants of the dynamics of the excitatory and inhibitory population respectively. $c_\bullet$'s are the coupling parameters between the two population. Coefficients $k_\bullet$ and $r_\bullet$ result from a temporal coarse-graining procedure in the initial derivation (see [42] for detail). $\mathscr{S}_\bullet$ is a sigmoidal transfer function, rising monotonically from 0 to 1 with non-negative input. P and Q are external inputs to their respective populations. If we divide both sides of equation 8-9 by the time constants, we are looking at the same general form as equation 1-2.

The main difference is between the respective transfer functions. Wilson and Cowan [42] chose a particular form of $\mathscr{S}$ for mathematical analysis:

$$\mathscr{S}(x) = \frac{1}{1 + \exp[-a(x - \theta)]} - \frac{1}{1 + \exp(a\theta)}, \tag{10}$$

where parameter a determines the maximal slope of the function $\mathscr{S}$ and parameter θ the location of the maximal slope. Technically, Wilson and Cowan [42] only requires

6

$\mathscr{S}$ to be of a general sigmoidal form. It may reflect the average response of a population of neurons with heterogeneous firing thresholds or heterogeneous afferent connections. The distribution of the said thresholds or connections is reflected in the parameters a and θ.

In other words, the choice of the transfer function and the parameters is *non-specific* to a predefined microscopic model. Moreover, Wilson and Cowan [42] took a function-oriented approach to analyzing the model. The key was whether the model was able to produce fundamental behaviors expected from a neural model— multistability, hysteresis, and oscillation—for *some* specific choice of parameters and transfer function. Qualitative conclusions from their analysis depend on the general geometric properties of the transfer function rather than the specific form of equation 10.

The transfer function of the present model (equation 3) follows the general geometric properties assumed by Wilson and Cowan [42]. The difference is that the parameters in equation 3 are associated specifically with a microscopic model [57], a network of leaky integrate-and-fire neurons with biologically plausible parameters, as inherited from the reduced Wong-Wang model [8, 44]. This choice provides a channel of correspondence between parameters of the models at different scales of description. To expand on this point, we next elaborate on the connection between the present model and the reduced Wong-Wang model.

2.3 Relation to the reduced Wong-Wang model

The present model is also a variant of the Wong-Wang model [44] and its high-dimensional generalizations, here referred to as the reduced Wong-Wang model [7–9]. In particular, we consider the model of whole-brain dynamics [8, 9],

$$\frac{\mathrm{d}\,S_E^{(i)}(t)}{\mathrm{d}\,t} = -\frac{S_E^{(i)}}{\tau_E} + \left(1 - S_E^{(i)}\right)\gamma_E\tilde{H}_E\left(w_{EE}^{(i)}S_E^{(i)} - w_{IE}^{(i)}S_I^{(i)} + I_G^{(i)}(\vec{S}_E)\right) + \sigma\xi^{(i)}(t) \tag{11}$$

$$\frac{\mathrm{d}\,S_I^{(i)}(t)}{\mathrm{d}\,t} = -\frac{S_I^{(i)}}{\tau_I} + \tilde{H}_I\left(w_{EI}^{(i)}S_E^{(i)} - w_{II}^{(i)}S_I^{(i)} + I_I\right) + \sigma\xi^{(i)}(t), \tag{12}$$

following the same notations as in equation 4-6, where

$$\tilde{H}_p(x) = \frac{a_p x - b_p}{1 - e^{-d_p(a_p x - b_p)}} \tag{13}$$

with $p \in \{E, I\}$ denoting the excitatory and the inhibitory population respectively (see Figure 2 dashed line for $\tilde{H}_E$). The parameters a_p, b_p and d_p were chosen such that $\tilde{H}_p$ approximates the average firing rate of an ensemble of leaky integrate-and-fire neurons receiving uncorrelated noisy inputs.

More specifically, the sub-threshold dynamics of the membrane potential $V(t)$ of each neuron can be described as

$$C_m\frac{\mathrm{d}\,V(t)}{\mathrm{d}\,t} = -g_L\left(V(t) - V_L\right) + I_{syn}(t) \tag{14}$$

where C_m is the membrane capacitance, g_L the leak conductance, and V_L the resting potential of the membrane. The total synaptic input current $I_{syn}(t)$ is a random process with an average μ_C and standard deviation σ_C. When $V(t)$ reaches a threshold V_{th}, the neuron emits a spike after which the membrane potential returns to a reset voltage V_{reset} and stays there for a duration τ_{ref}, i.e. the refractory period.

The average firing rate ν of an ensemble of such neurons can be derived from the Fokker-Planck approximation that describes the evolution of the membrane voltage distribution of an ensemble of neurons (see e.g. [64, Section 1], [56] for descriptions

7

of the Fokker-Planck approach). This eventually leads to the first-passage time equation (average time for crossing the threshold),

$$\nu = \left(\tau_{\mathrm{ref}} + \tau_m \sqrt{\pi} \int_{\frac{V_{\mathrm{reset}} - V_{\mathrm{ss}}}{\sigma_V}}^{\frac{V_{\mathrm{th}} - V_{\mathrm{ss}}}{\sigma_V}} e^{x^2}(1 + \mathrm{erf}(x)) dx \right)^{-1} \tag{15}$$

where $\tau_m = C_m/g_L$ is the membrane time constant, $\sigma_V = \sqrt{\tau_m}\sigma_C/C_m$ the standard deviation of the depolarization, $\mathrm{erf}(x)$ the error function

$$\mathrm{erf}(x) = \frac{2}{\sqrt{\pi}} \int_0^x e^{-u^2} du, \tag{16}$$

and V_{ss} the steady state voltage

$$V_{\mathrm{ss}} = V_L + \frac{I_{syn}}{g_L}. \tag{17}$$

The transfer function employed by Wong and Wang [44, 63], i.e. equation 13 with appropriate choice of parameters, is a good approximation of equation 15 when the input level is low.

Thus, the first passage equation 15 provides a bridge between the transfer function (equation 13) and the single-cell level model (equation 14) incorporating realistic biophysical parameters (Table 2). In other words, it allows one to use empirically measurable quantities at the neuronal level to directly constrain the the transfer function and the entire model. This is a major difference with the Wilson-Cowan model [42, 43].

parameter	interpretation	value
C_m	membrane capacitance	0.5, 0.2 (nF)
g_L	leak conductance	25, 20 (nS)
τ_m	membrane time constant	20, 10 (ms)
τ_{ref}	refractory period	2 (ms)
V_L	resting membrane potential	-70 (mV)
V_{th}	threshold for firing	-50 (mV)
V_{reset}	reset potential	-55 (mV)

Table 2: **Biophysical parameters of a single leaky-integrate-and-fire neuron.** If two parameter values are provided in the right column, the first value is for a generic pyramidal cell and the second is for a generic interneuron. Differences between the biophysical parameters of different cell types lead to differences in the transfer functions (equation 13).

According to the first passage equation 15, the firing rate ν is a sigmoidal function of the input, which saturates at $r_{max} \equiv 1/\tau_{ref}$. This is not the case, however, for the transfer function $\tilde{H}$ (equation 13). To make the transfer function a better approximation of the first passage equation and at the same time retain the mapping between their parameters, we can simply convert the transfer function by substituting the numerator of $\tilde{H}$ as below

$$H_p(x) = \frac{r_{max} - \tilde{H}_p(r_{max} - x)}{1 - e^{-d_p(a_p x - b_p)}}. \tag{18}$$

Thus, we obtain the transfer function used in the present model (equation 3). As shown in Figure 2, H_p matches $\tilde{H}_p$ for low levels of input but flattens out eventually at r_{max} as one would expect from equation 15.

In short, the present model is endowed with the geometric properties of the Wilson-Cowan model [42, 43] and at the same time consistent with the neuronal level-to-population level mapping of the reduced Wong-Wang model [8, 44].

8

2.4 Data and methods of analysis   193

2.4.1 Human structural data   194

The human structural connectome used in the present study is an average of   195
the connectome of 11 unrelated subjects (the S1200 Release) from the Human   196
Connectome Project (HCP) [59]. The subject-level connectome data are based on   197
the Desikan-Killiany parcellation [65] obtained from [60], retaining the 66 ROIs   198
used in [58] and [7] (Figure 1b). The original diffusion imaging (dMRI) data were   199
obtained using a customized Siemens 3T scanner at Washington University in St.   200
Louis, with a standard 32-channel head coil, with TR = 5520 (ms), TE = 89.5   201
(ms), 1.25 (mm) isotropic voxels, b=1000, 2000, 3000 (s/mm^2). T1 images were   202
obtained using 3D magnetization-prepared rapid gradient echo sequence (MPRAGE)   203
with TR = 2400 (ms), TE = 2.14 (ms), and 0.7 (mm) isotropic voxels. The HCP   204
minimally processed data were further processed using *MRtrix3*, including bias-   205
field correction, multi-shell multi-tissue constrained spherical deconvolution with   206
a maximum spherical harmonic degree 8. 10 million probabilistic streamlines were   207
generated for each subject using the 2nd-order Intergration over Fibre Orientation   208
Distributions algorithm (iFOD2) [66] and anatomically-constrained tractography   209
(ACT) [67] (FOD amplitude threshold = 0.06, step size = 0.625 mm). Each streamline   210
was assigned a weight using spherical-deconvolution informed filtering of tractograms   211
(SIFT2) [68]. Connection strengths between ROIs are summed weights of the   212
associated streamlines. Intra-ROI connections are removed. Subjects' connectivity   213
matrices are normalized according to equation 7 before and after averaging.   214

2.4.2 Human functional data   215

Human functional connectivity used in the present study is estimated using the   216
resting-state fMRI (rfMRI) data of the same 11 unrelated subjects from the Human   217
Connectome Project [59] as the structural connectivity above. rfMRI scans were   218
acquired using EPI sequences with TR = 720 (ms), TE = 33.1 (ms), flip angle =   219
52°, voxel size = 2.0 (mm, isotropic), multiband factor = 8. Four runs of rfMRI   220
scan were obtained from each subject in 2 separate days (2 runs in each day with   221
opposite phase-encoding direction: RL and LR). Each run last 14 min 33 s (1200   222
TR).   223

Unprocessed data were downloaded from the Human Connectome Project   224
database (https://db.humanconnectome.org) and preprocessed using *fMRIPrep*   225
1.4.0 ([69]; [70]; RRID:SCR_016216), which is based on *Nipype* 1.2.0 ([71]; [72];   226
RRID:SCR_002502). First, a reference volume and its skull-stripped version were   227
generated using a custom methodology of *fMRIPrep*. A deformation field to cor-   228
rect for susceptibility distortions was estimated based on two echo-planar imaging   229
(EPI) references with opposing phase-encoding directions, using `3dQwarp` [73] (AFNI   230
20160207). Based on the estimated susceptibility distortion, an unwarped BOLD   231
reference was calculated for a more accurate co-registration with the anatomical   232
reference. The BOLD reference was then co-registered to the T1w reference us-   233
ing `bbregister` (FreeSurfer) which implements boundary-based registration [74].   234
Co-registration was configured with nine degrees of freedom to account for dis-   235
tortions remaining in the BOLD reference. Head-motion parameters with respect   236
to the BOLD reference (transformation matrices, and six corresponding rotation   237
and translation parameters) are estimated before any spatiotemporal filtering using   238
`mcflirt` [FSL 5.0.9, 75]. The BOLD time-series, were resampled to the *fsaverage*   239
surface space. Several confounding time-series were calculated including framewise   240
displacement (FD), DVARS and three region-wise global signals. FD and DVARS   241
were calculated for each functional run, both using their implementations in *Nipype*   242
[following the definitions by 76]. The three global signals were extracted within the   243
CSF, the WM, and the whole-brain masks.   244

Nuance regressions were performed on detrended, preprocessed BOLD time series   245

9

in the *fsaverage* space (FreeSurfer), following procedures in [76]. Regressors include 6 motion parameters, CSF signal, WM signal, and their first derivative and second power. Frames with FD>0.2 mm are censored. Spline-interpolated signals are band-pass filtered between 0.009 and 0.08 Hz, and averaged within ROIs based on Desikan-Killiany parcellation [65]. 66 Regions in [58] are retained and ordered according to [7] (Figure 1b). Functional connectivity between ROIs are estimated using Spearman correlation between z-scored time series for each rfMRI run of each subject. The connectivity matrices are then averaged across all runs/subjects in Day 1 and in Day 2 separately. The average functional connectivity matrix from Day 1 is used in all comparisons with the model. The average functional connectivity matrix from Day 2 is used to assess the reliability of the estimation.

2.4.3 Model inter-regional coordination

Two types of inter-regional coordination in the model are computed and compared to the human functional connectivity. One estimates how every two model regions move together across different attractors throughout the entire dynamic landscape, namely *cross-attractor coordination*. The other estimates how two model regions move together during noise-driven exploration near a single attractor, namely *within-attractor coordination*.

For cross-attractor coordination, the attractors are first discretized by replacing the state of each region with an integer, determined by a 30-bin histogram of regional states $S_E^{(i)}$ (Section S3). This procedure allows us to quantify whether two regions move up and down together across different attractors without considering the distance between attractors and the continuous shift of the position of each attractor. The cross-attractor coordination between region x and y is computed as the Spearman correlation (ρ) of their discrete states across a fixed set of attractors, determined by structural parameters G, w_{EE}, and w_{EI} (see Figure 6 for a conceptual illustration). Note that this procedure only requires the coordinates of each attractor through, e.g. the computation of a bifurcation diagram (Section S1)—simulation of the time series is not required. The distance between attractors is computed separately as the difference between the average state of the excitatory population $\bar{S}_E$, which can be interpreted as the energy cost associated with keeping additional x% synaptic channels open. Within-attractor coordination is the Spearman correlation between simulated time series of the excitatory population of region x and y, given an initial condition right at an attractor, a moderate level of noise $\sigma = 0.01$ and a duration $T = 864$ s (14 min 33 s to match the human data).

3 Results

In the following sections, we first examine the dynamic repertoire of isolated brain regions (the local model; Section 3.1) and how nonlinearity in the present model enhances multistability and produces realistic oscillations (Section 3.2). We further show how long-range connectivity between these brain regions interacts with local properties in shaping global multistable landscapes (Section 3.3), human functional connectivity patterns (Section 3.3), and temporal diversity across regions (Section 3.4). The numerical results are illustrated in the main text while the corresponding analytical supports are provided in the Supplementary Materials.

10

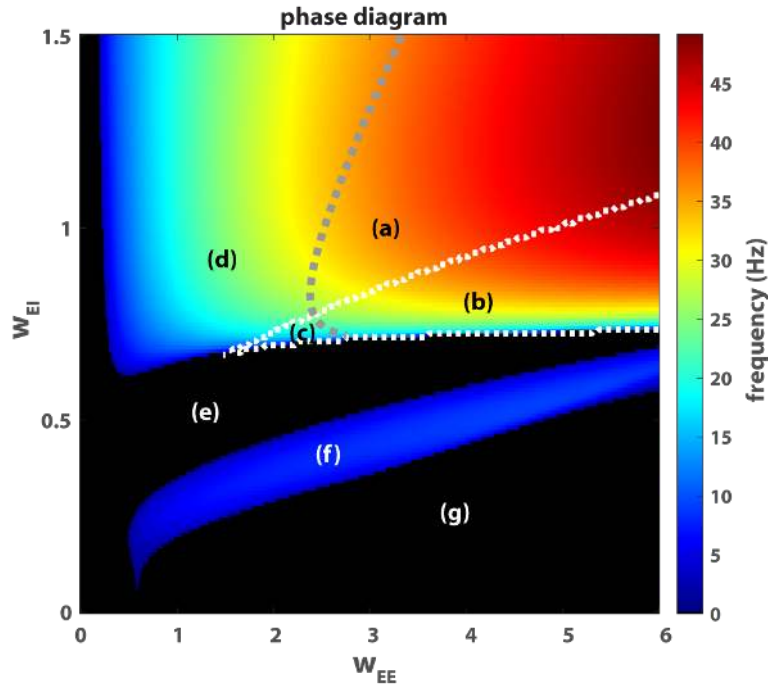### 3.1 Local structural connectivity controls dynamic repertoire of an isolated brain region

Figure 3: **Local dynamics controlled by the strength of excitatory-to-excitatory connection w_{EE} and excitatory-to-inhibitory connection w_{EI}.** (a)-(g) are seven different dynamic regimes of the local model (equation 1-2) in the 2-dimensional parameters space (w_{EE}, w_{EI}). Here the local inhibitory-to-excitatory connectivity w_{IE}—the inhibitory feedback—is matched to the excitatory-to-excitatory connectivity, i.e. $w_{IE} = w_{EE}$; and $I_E = 0.382$ as in [8]. Black areas (e, g) are the regimes of stable equilibrium. Colored areas are the oscillatory regimes: (a)-(b) for limit cycles and (c), (d), (f) for damped oscillations. The color reflects the frequency of oscillation. A gray dashed line indicates the Hopf bifurcation. The triangular area enclosed by white dashed lines (saddle-node bifurcation) is the bi-stable regime (b, c). A typical phase portrait from each regime is provided in Figure 4.

The local model exhibits a rich repertoire of dynamical features, including multistability (b, c in Figure 3, 4), damped oscillation (c, d, f), and limit cycles (sustained oscillation; a, b). Mathematical analysis of the local model (Section S7 in Supplementary Materials) shows that nonlinearity in the dynamics can essentially be controlled by two local structural properties: the strength of excitatory-to-excitatory connection w_{EE} and the strength of the excitatory-to-inhibitory connection w_{EI}. Geometrically, the two structural properties "twist" the nullclines (dashed lines in Figure 4). Specifically, stronger w_{EE} introduces a deeper twist and fold of the red nullcline (compare Figure 4a and d), whereas stronger w_{EI} introduces a more vertical twist of the blue nullcline (compare Figure 4d and e). These twists are the key sources of dynamic complexity—multistability and oscillation. For example, when w_{EE} is sufficiently large (equation S19), multistability becomes possible: the folded red nullcline allows for multiple intersections with the blue nullcline, and potentially a greater number of attractors (compare Figure 4c to a; see analytical results in Section S7: Multistability). When w_{EI} is sufficiently large (equation S27), oscillatory activity becomes possible (analytical results in Section S7: Oscillation). Moreover, the combination of large w_{EE} and w_{EI} gives rise to sustained oscillation

11

(equation S50). The characteristic frequency of such oscillation further depends on the specific values of w_{EE} and w_{EI}. Note that the general qualitative effects of these two local structural properties are consistent with those of the Wilson-Cowan model, but the specific boundaries at which transitions occur are determined by the biophysical constraints inherited from the reduced Wong-Wang model (see equations S27, S50). Analytical results (Section S7) provide detailed quantification of how these boundaries are shifted by different local structural properties.

To maintain a sufficient twist in the red nullcline (red dashed line in Figure 4) and associated multistability and oscillation, inhibitory-to-excitatory feedback w_{IE} needs to be proportional to self-excitation w_{EE} (c.f. equation S9). In the present study, we simply let $w_{IE} = w_{EE}$. This equality is a simpler alternative to the Feedback Inhibition Control adopted in [8] in both numerical and mathematical analyses.
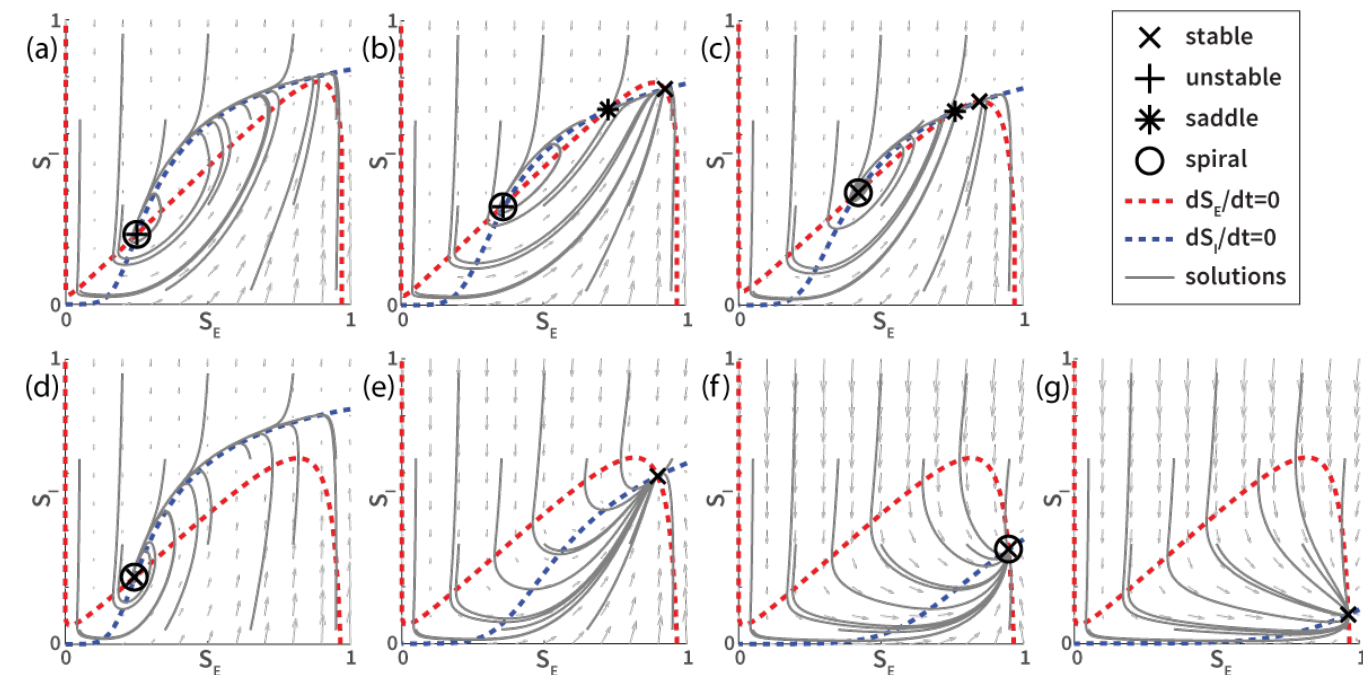
Figure 4: **Example phase portraits from different regimes of the local model**. Phase portraits (a) to (g) are examples chosen from the corresponding regimes in Figure 3. The specific parameters defining local structural connectivity are (a) $w_{EE} = 4$, $w_{EI} = 1$; (b) $w_{EE} = 4$, $w_{EI} = 0.8$; (c) $w_{EE} = 2.3$, $w_{EI} = 0.75$; (d) $w_{EE} = 1.5$, $w_{EI} = 1$; (e) $w_{EE} = 1.5$, $w_{EI} = 0.5$; (f) $w_{EE} = 1.5$, $w_{EI} = 0.3$; (g) $w_{EE} = 1.5$, $w_{EI} = 0.2$. The vector fields (arrows) reflect the underlying dynamics at different points in the state space. Gray trajectories following the vector fields are solutions of the local model (equation 1, 2) given a fixed sets of ten different initial conditions. Nullclines (dashed lines) indicate where the flow of the dynamics is either purely vertical (red) or purely horizontal (blue). The intersections between the nullclines are the fixed points. Different types of fixed points are labeled with different markers (see legend). A fixed point is stable ($\times$) if nearby trajectories converge to it over time, unstable ($+$) if nearby trajectories diverge from it, or a saddle ($*$) if nearby trajectories approach it in some direction(s) but diverge from it in some other direction(s). A fixed point is said to be a spiral ($\circ$) if trajectories near the fixed point rotate either towards the fixed point (damped oscillation) or away from the fixed point (sustained oscillation or limit cycle in the present case). Strong oscillation mainly appears on the ascending branch of the red nullcline. Overall, we see that local connectivity defines the dynamics in each regime essentially by controlling the geometry of the nullclines.

3.2 The effects of nonlinearity in the local model

Before getting into the global model, we briefly demonstrate numerically how the present unified model (equation 1-2) extends the reduced Wong-Wang model [8, 44] to more complex scenarios. As expected, the dynamics of the present model match that of the reduced Wong-Wang model for low levels of excitation, i.e. weak local excitatory connectivity (Figure 5a-b). In a regime of stronger local excitatory connectivity, as explored in [9], the two models diverge (Figure 5c-d). In the present model (Figure 5c), all trajectories are well-confined within a physiologically plausible range—state variables S_E and S_I denote the fraction of open channels, which by definition are between 0 and 1. In contrast, certain trajectories of the reduced Wong-Wang model (Figure 5d) overshoot beyond the physiologically plausible range. The effect of added nonlinearity in the present model manifests through the curvature of the blue nullclines, which confines the flow of oscillatory activities and creates extended multistability (see e.g. Figure 4b). Thus, the present model is more suitable for studying key nonlinear dynamical features in the resting brain.
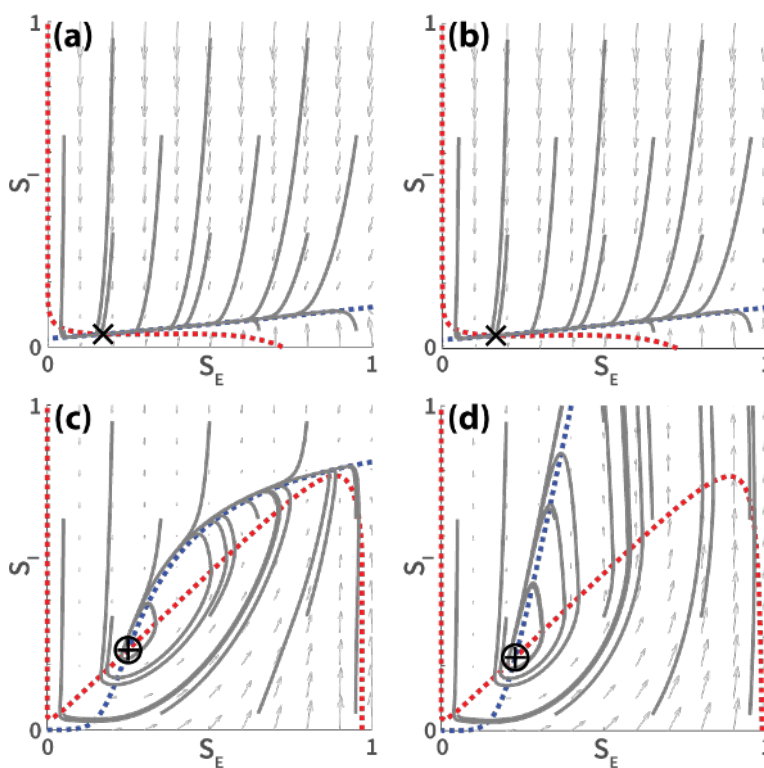

Figure 5: **Comparisons between the present unified model (a, c) and the reduced Wong-Wang model (b, d) in two dynamic regimes.** (a) and (b) show the phase portraits of the present model (equations 1-2) and the reduced Wong-Wang model (equations 11-12) respectively in a regime of weak local excitatory connectivity. Parameter values are obtained from [8] and identical across the two models: $w_{EE} = 0.21$, $w_{EI} = 0.15$, $w_{IE} = 1$, $w_{II} = 1$, $I_E = 0.382$ and $I_I = 0.267$ (unspecified parameters follow Table 1). The resulted dynamics are virtually identical. (c) and (d) show a similar comparison between the two models in an oscillatory regime, where the local excitatory connectivity is stronger ($w_{EE} = 4$, $w_{EI} = 1$). While the dynamics of the present model (c) is well confined within a realistic range (S_E, $S_I \in [0,1]$), it is not the case for the reduced Wong-Wang model (d).

13

3.3 Multistable landscape of the brain shaped by structural properties across scales

In Figure 6, we provide basic intuitions about dynamic landscapes and their repertoire of attractors as a system-level description of intrinsic brain dynamics. An attractor in the global model represents a stable pattern of activation over the whole brain (black boxes in Figure 6). The dynamic landscape of the brain (Figure 6a-c) defines the repertoire of attractors, thereby possible patterns of activity (e.g. a1-a4), paths of transitions (black arrows), and the coordination between brain regions during transitions (2-by-2 matrices). As the landscape itself changes, some attractors may be destroyed (Figure 6, a→b, or a→c) or created (b→a, c→a)—a discrete change of the repertoire called bifurcation. In the present model, local and global structural connectivity control the shape of the landscape, and thereby, the repertoire of attractors, possible transitions, and associated inter-regional coordination.
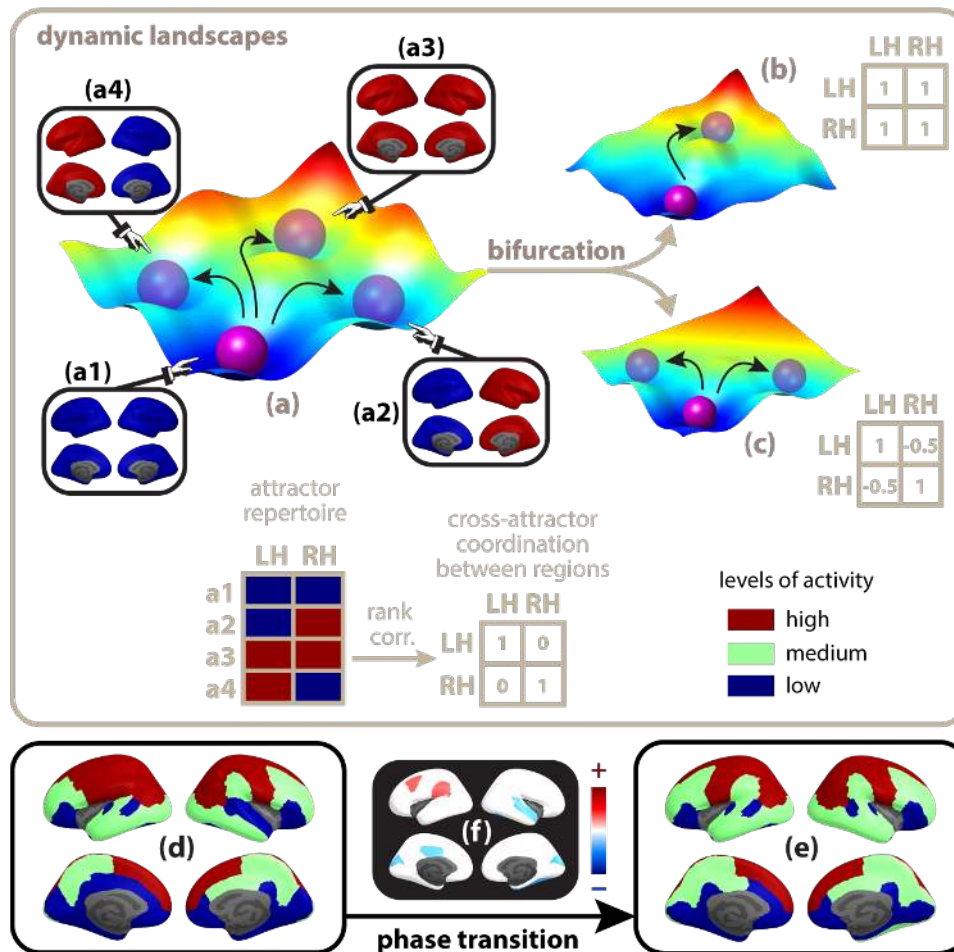
14

Figure 6: **Conceptual illustration of the whole-brain dynamic landscape, bifurcation, and phase transition.** A multistable dynamic landscape (a) contains multiple attractors, shown as troughs occupied by purple balls. For the present model, each attractor is interpreted as a distinct pattern of activation over the whole brain (a1-a4). Influenced by external input or intrinsic noise, the model brain may transition from its current state (a1, bright purple ball) to a different one (a2, a3, or a4, dim purple balls), indicated by black arrows. Structural properties of the model brain can alter the shape of the landscape, causing some attractors to appear or disappear through a process mathematically named bifurcation (a→b, a→c, or the reverse). By modifying the repertoire of attractors, bifurcation alters the set of possible transitions and the coordination between regions during transitions: in landscape (a), the left and right hemisphere can be co-activated during a transition (a1→a3), or activated independently through other transitions (a1→a2, or a1→a4); in contrast in landscape (b), the left and right hemisphere can only be co-activated, and in (c), only activated independently. Numerically, a repertoire of attractors can be represented as a matrix, where each row is an attractor and each column is a brain region (e.g. the 4-by-2 matrix below landscape a, for 4 attractors – a1-a4, and 2 regions – left and right hemisphere). Overall cross-attractor coordination between regions can be estimated by rank correlation between the columns of the repertoire matrix. The resulted square, coordination matrix summarizes how brain regions transition together over the entire landscape, serving as a signature of the landscape (e.g. 2-by-2 matrices next to a-c). In more complex landscapes (not shown), there are many more attractors, and they correspond to subtler patterns of activation (d,e; see also Figure 7). The coordination between brain regions during a transition is correspondingly more complex (f=d-e), with some regions co-activated (red) while others co-deactivated (blue).

15

Figure 7 shows such dynamic landscapes and their changes more abstractly as bifurcation diagrams (see Section S1 for computational details). In each bifurcation diagram, the y-coordinate of each *colored* point indicates the position of an attractor by an order parameter (e.g. average activity of all excitatory populations $\bar{S}_E$), and x-coordinate a control parameter that modulates the shape of the underlying dynamic landscape (e.g. global coupling G in equation 6). Each vertical slice of a bifurcation diagram contains the repertoire of attractors and repellers in a fixed landscape (Figure 7h), corresponding to stable and unstable patterns of brain activity. Horizontal stripes are formed when an attractor changes continuously with the landscape, but destroyed when they merge with a black stripe (unstable patterns) at a bifurcation. Thus, the number of colored stripes reflect the complexity of the landscapes: more stripes, more attractors.

In the simple case where all brain regions are connected to each other at the same strength (uniform connectivity; Figure 7d-f), stronger local excitatory connection (e,f) produces a more complex landscape (3 attractor stripes) than a weak one (d; 2 attractor stripes). These bifurcation diagrams are very similar to those of a single brain region (Figure 7a-c), in terms of the number of attractors and the presence oscillation. In fact, the whole brain (Figure 7e) moves up and down together between discrete state of activation very much like a single region (Figure 7b). One remarkable difference between the uniformly connected global models and the corresponding local models is that, with the absence of persistent input, the global model can retain memories of prior input while the local model cannot. That is, when input $I_E = 0$, the local model is monostable (bottom red stripes in Figure 7a-c), i.e. returning to the same state regardless of prior input. The global model (equation 4-6) by definition does not receive external input; yet the model is multistable for a sufficient amount of global coupling, e.g. $G > 1$ (Figure 7d-f). We further substantiate and generalize this result analytically and numerically (Section S8 Multistability) to the case where each isolated brain region is monostable for any I_E. These findings suggest that the coupling between brain regions can synergistically create a functional repertoire or memory capacity that isolated brain regions do not possess.

Given a realistic global structural connectivity (human connectome; Figure 7g-i), the complexity of the whole-brain dynamic landscape is dramatically increased: 171 attractor stripes in (g), 610 in (h), and 682 in (i) (per single-linkage clustering). Correspondingly, the patterns of activation (Figure 7f) are also more complex, with greater differentiation between regions; the coordination between brain regions across attractors is consequently more flexible and subtle (Figure 6f). The heterogeneous nature of the human connectome breaks the large-scale spatial symmetry of the model brain, creating more functional differentiation between brain regions and a greater functional complexity for the whole brain. In short, the complexity of the global dynamical landscape is a joint product of strong local excitatory connection and complex topology of the large-scale network. See Section S8 for additional analytical supports.
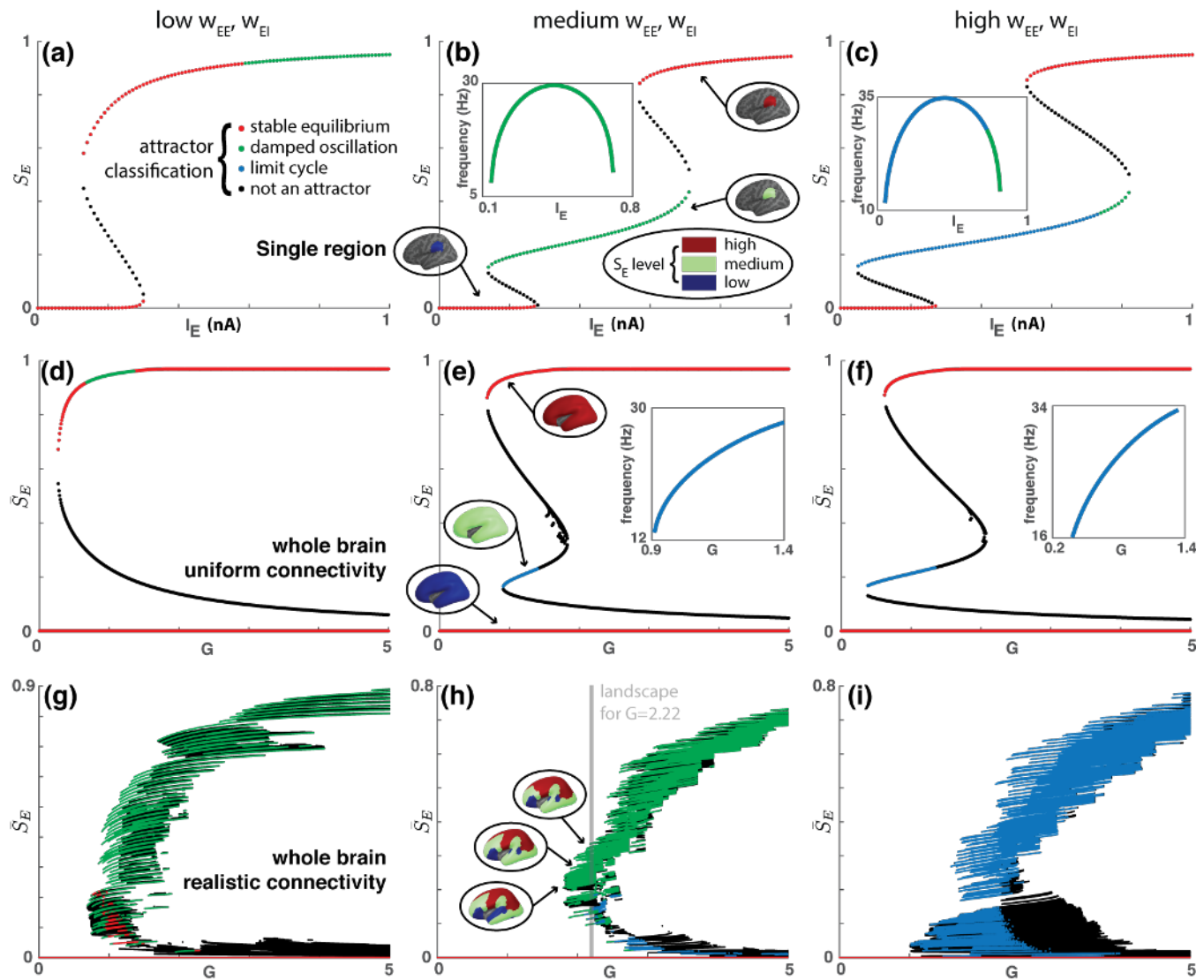
16

Figure 7: **Local and global structural properties jointly determine the complexity of whole-brain dynamics.** (a-c) show the bifurcation diagrams of the local model for three different types of local excitatory connectivity: (a) $w_{EE} = 0.7$ and $w_{EI} = 0.35$; (b) $w_{EE} = 2$ and $w_{EI} = 1$; (c) $w_{EE} = 2.8$ and $w_{EI} = 1$. Overall, local connectivity increases from (a) to (c). The activity of the excitatory population S_E is used as an order parameter, indicating the location of each attractor. The external input I_E is used as a control parameter. Each point in the diagram indicates the location of a particular fixed point. The color denotes the type of each fixed point: non-black points represent attractors, black points unstable fixed points that are not associated with a limit cycle. Horizontal stripes indicate that the attractors are changing continuously with the control parameter for a certain range. All (a)-(c) have a upper stripe and a lower stripe. (b)-(c) have an additional stripe in the middle, where the brain region oscillates. Insets of (b) and (c) show the oscillation frequency of the brain region as a function of the input current. Each stripe corresponds to a discrete level of activation for a single brain region (circled brains in b; color indicates discrete S_E levels, shown in circled legend). (d)-(f) show the corresponding bifurcation diagrams for three uniform global networks, i.e. the large-scale structural connectivity C_{ij}'s are identical between any two brain regions $i \neq j$ (equation 6). The average activity of all excitatory populations ($\bar{S}_E$) is used as an order parameter and the global coupling G (equation 6) as an control parameter. Each attractor stripe corresponds to a pattern of activation over the whole brain (circled brains in (e) show $S_E^{(i)}$'s on the left hemisphere). Similarly, (g)-(i) show the corresponding bifurcation diagrams for three realistic global networks, i.e. C_{ij}'s reflect the human connectome (see text for details). Here each vertical slice (gray line in h) contains the attractor repertoire of a fixed dynamic landscape shaped by the human connectome. Each attractor repertoire is associated with a matrix describing the coordination between brain regions across attractors (e.g. Figure 8b). See Figure 6 for a cartoon illustration of an attractor repertoire and its associated cross-attractor coordination matrix.

17

What do these complex landscapes say about the dynamics in the human brain? Below we show that large-scale functional connectivity patterns in human fMRI data (Figure 8a) can be aptly explained by how brain regions transition together across attractors—*cross-attractor coordination* (Figure 8b), better than how they coordinate within any single basin of attraction—*within-attractor coordination* (Figure 8c).

Human functional connectivity (Figure 8a) is calculated from the resting fMRI data from the Human Connectome Project [59], averaged across the same subjects whose structural connectome is incorporated in the model (Figure 8e; see Section 2.4 and Section S4 for more details). The human functional connectivity exhibits large-scale symmetry across two hemispheres. That is, functional connectivity within the right hemisphere is similar to the connectivity within the left hemisphere (compare upper-left and lower-right block in Figure 8a), and similar to the connectivity across the left-right hemispheres (compare upper-left and lower-left block in Figure 8a). This dominant feature of human resting brain dynamics is well preserved in the model by the cross-attractor coordination between model regions (Figure 8b; see Section 2.4.3 for detail, Figure 6a-c for intuition regarding cross-attractor coordination). Quantitatively, this is also reflected as the consistent model fit for both intra- and inter-hemispheric connectivity (dashed lines in Figure 8d; black dashed line: whole-brain fit, $\rho = 0.591$, $p < 0.001$, $R^2 = 0.349$; red dashed line: intra-hemispheric fit, $\rho = 0.582$, $p < 0.001$, $R^2 = 0.338$; blue dashed line: inter-hemispheric fit, $\rho = 0.604$, $p < 0.001$, $R^2 = 0.364$), and across model parameters (Figure 9a-c).

The above finding paints a rather different picture than previous theories in which the resting brain is thought to explore the dynamic landscape near a single attractor, delicately poised near a bifurcation (e.g. [7, 9]). For comparison, we simulated functional connectivity within each of the individual attractors involved in cross-attractor coordination. The best-fit within-attractor coordination matrix is shown in Figure 8c ($\rho = 0.463$, $p < 0.001$, $R^2 = 0.190$), clearly missing the symmetry between intra- and inter-hemispheric connectivity observed in humans (Figure 8a) and cross-attractor coordination of the model (Figure 8b). Moreover, within-attractor coordination does not capture inter-hemispheric connectivity in humans as well as intra-hemispheric connectivity (solid lines in Figure 8d), and overall fits worse than cross-attractor coordination (dashed lines in Figure 8d; for comparison, best-fit intra-hemispheric within-attractor coordination gives $\rho = 0.534$, $p < 0.001$, $R^2 = 0.285$). The distinction between within- and cross-attractor coordination is more drastic when the contribution of structural connectivity is controlled using partial correlation (Figure 8f; contrast best-fit within-attractor intra-hemispheric coordination: $\rho = 0.218$, $p < 0.001$, $\Delta R^2 = 0.0269$, $F(1, 1053) = 52.3$, v.s. cross-attractor intra-hemispheric coordination: $\rho = 0.417$, $p < 0.001$, $\Delta R^2 = 0.0991$, $F(1, 1053) = 221$). These findings suggest that cross-attractor coordination better captures features of human resting brain dynamics that are unexplained, linearly, by the structure.

18

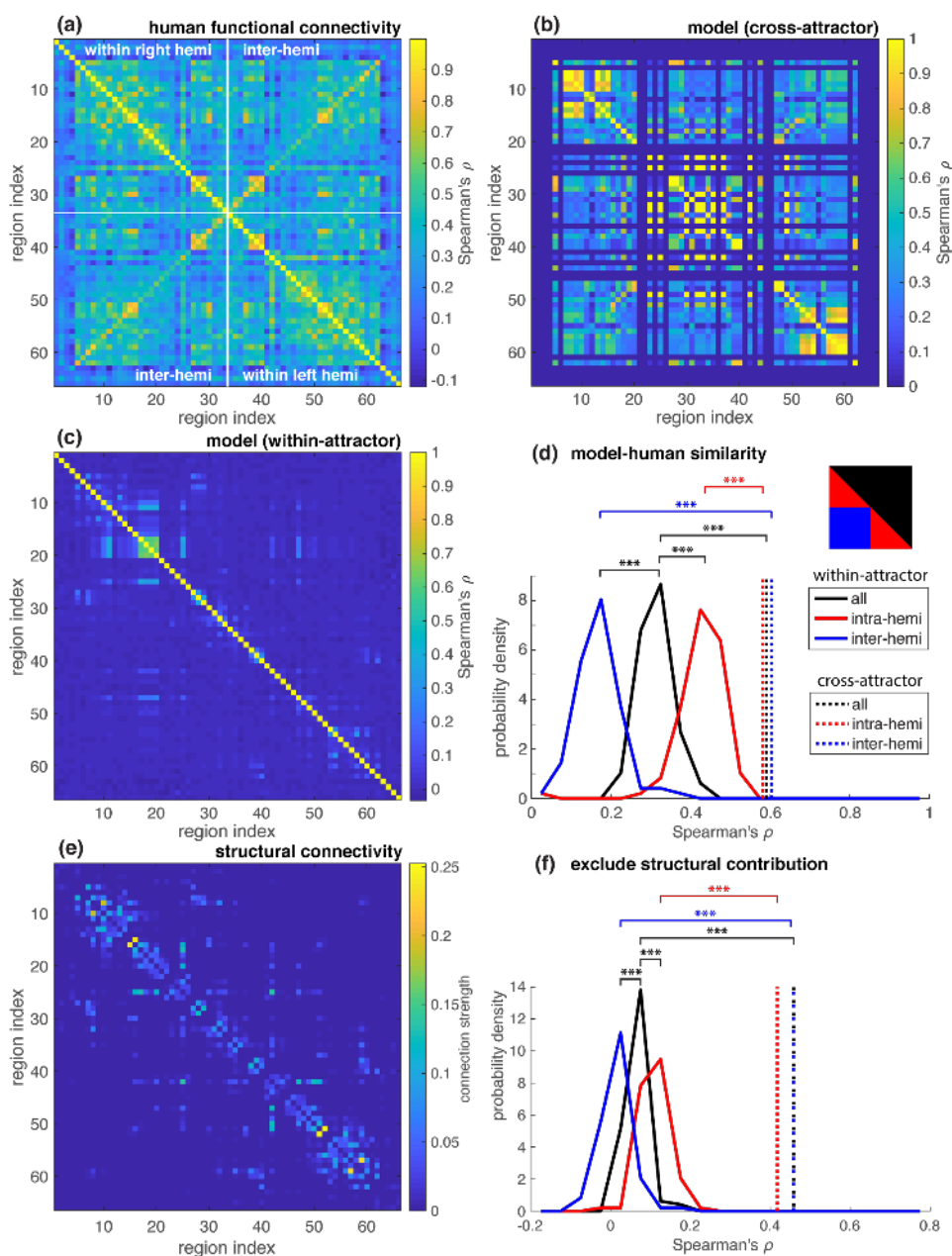Figure 8: **Human resting functional connectivity better captured by cross-attractor, rather than within-attractor, coordination between model brain regions.** Human functional connectivity matrix (a) is calculated using the resting fMRI data from the Human Connectome Project [59], averaged over the same subjects whose average structural connectome defines the long-range structural connectivity in the model (e). Regions (columns and rows) are ordered symmetrically for the left and right hemisphere (see Figure 1b) to reveal the large-scale symmetry of resting brain dynamics. White lines delineate the matrix (a) into four blocks, describing the functional connectivity within the right hemisphere (upper left block), within the left hemisphere (lower right), and between two hemispheres (lower left/upper right). Functional connectivity within the hemispheres are similar to each other (symmetric along anti-diagonal), and also similar to inter-hemispheric connectivity (symmetric along white lines). This large-scale functional symmetry is well captured by inter-regional coordination in the model brain ($w_{EE} = 2$, $w_{EI} = 1$, $G = 2.22$) across attractors (b; 97 attractors shown in Figure 7h for $G = 2.22$). Such symmetry is not captured by the coordination within any of the said attractors (c; best fit within-attractor coordination matrix). In (d), solid line shows the distribution of correlation coefficients between human functional connectivity (a) and within-attractor coordination matrices (not shown except c). All of which are lower than the correlation (dashed lines in d) between human functional connectivity (a) and the cross-attractor coordination matrix (b). (f) shows a similar comparison as (d) using partial correlation controlling the contribution of structural connectivity (e). (*** $p < 0.001$, Bonferroni corrected)
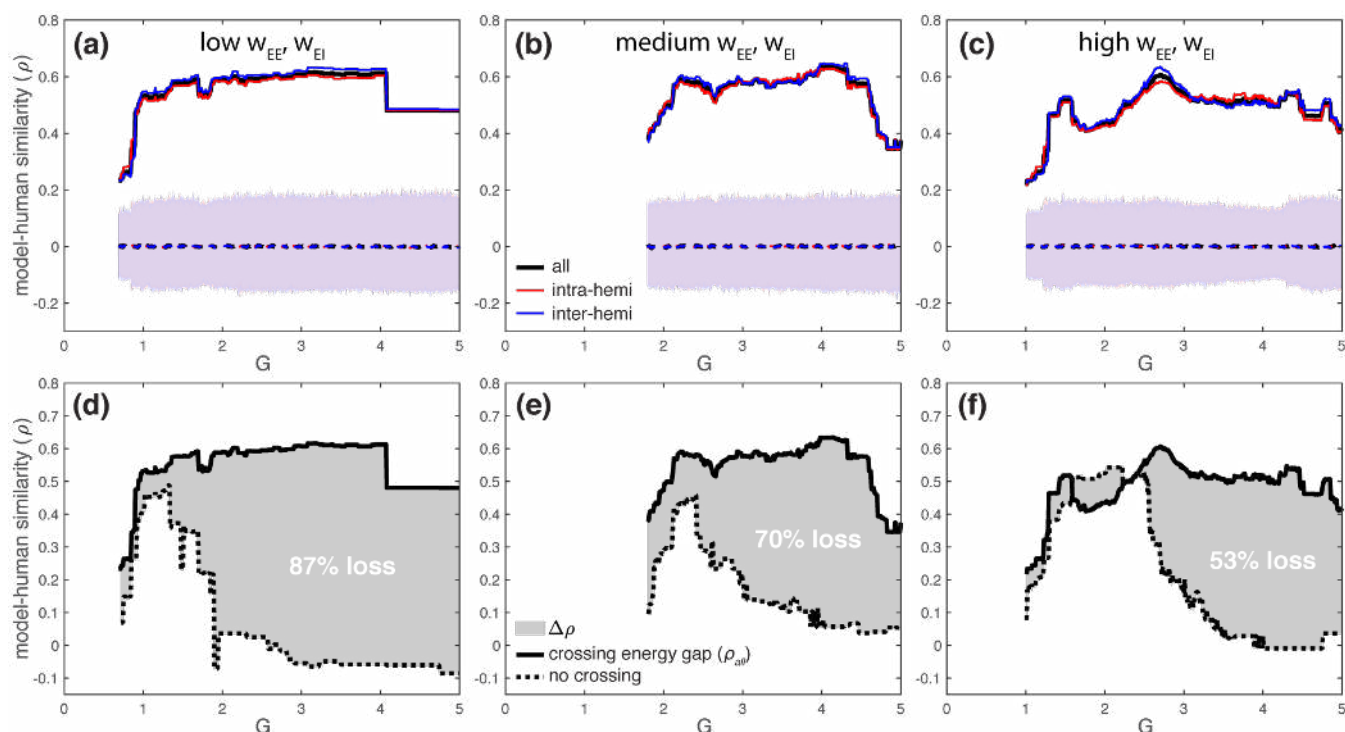
Figure 9: **Model-human similarity consistent for within- and cross-hemispheric coordination, affected by energy constraints.** (a-c) Cross-attractor coordination in the model is highly similar to human functional connectivity across different local excitatory connectivity: (a) $w_{EE} = 0.7$ and $w_{EI} = 0.35$, (b) $w_{EE} = 2$ and $w_{EI} = 1$, (c) $w_{EE} = 2.8$ and $w_{EI} = 1$, as in Figure 7. Red solid lines indicate the model-human similarity (Spearman correlation) for intra-hemispheric connectivity, blue ones for inter-hemispheric connectivity, black ones for whole-brain connectivity. Dashed lines and shaded areas indicate the means and 95% confidence intervals of the null distributions, constructed using 1000 random permutations of ROI labels (red, blue, black distributions are largely overlapping not visually distinguishable). Black solid lines in (d-f) are reproduced from (a-c) indicating the model-human similarity over the whole brain. Dashed lines in (d-f) indicate the model-human similarity when the model is not allowed to cross the largest energy gap between attractors. The shaded area ($\Delta \rho$) indicates the loss of similarity between the model and the humans.

As alluded to, cross-attractor coordination in the model captures human functional connectivity for a wide range of structural configurations (Figure 9a-c; see also Figure S3). Then, what roles do local (w_{EE}, w_{EI}) and large-scale structural properties (e.g. global coupling G) play in producing human-like functional connectivity? The answer lies in the energy gap between different attractors. In the computation of cross-attractor coordination matrices (e.g. Figure 8b, Figure 6a-c), we considered only whether two brain regions move up and down together across the dynamic landscape, not how difficult the movements are. In fact, the average of the pattern change ($\Delta \bar{S}_E$, e.g. Figure 6f) between attractors (e.g. Figure 6, d→e) reflects an energy gap — the energy needed to keep x% additional synaptic channels open. The similarity to human functional connectivity drops greatly if the model brain is not allowed to traverse the largest energy gap in the dynamic landscape (dashed lines in Figure 9d-f). This energy constraint has a greater impact on model-human similarity when the local structural connectivity is weaker (area of the shaded region grows from Figure 9d to f; bars in Figure 10) and the global structural connectivity is stronger (height of shaded regions grows with G in Figure 9d-f). The loss of similarity grows with the maximal gap size, especially for a gap size greater than 0.2 (Figure 10). Thus, local and global structural connectivity both influence the energy costs associated with cross-attractor coordination, and thereby how likely it is for human-like functional connectivity patterns to emerge under energy con-

433
434
435
436
437
438
439
440
441
442
443
444
445
446
447
448
449
450
451
452

straints. Overall, stronger local connection reduces the energy gaps (Figure 11a-c)   453
and stronger global connection (G) increases the energy gaps (Figure 11a)—local   454
and global structural connectivity pull the energy cost in different directions.   455
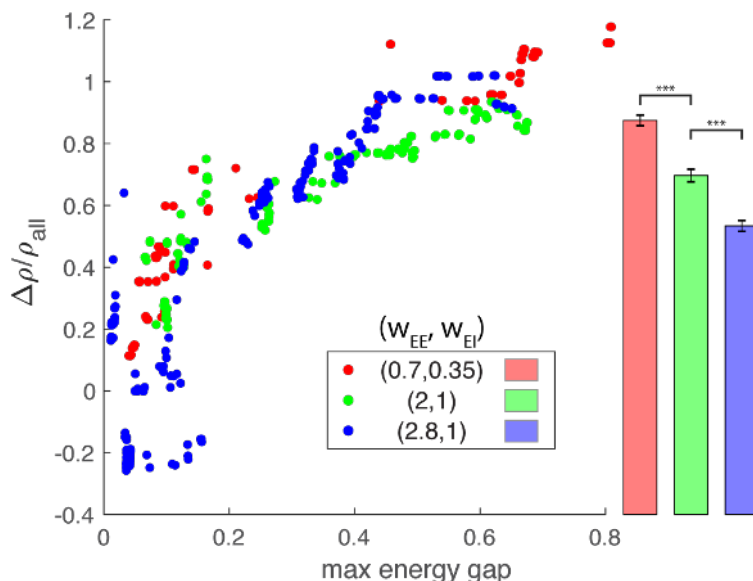

Figure 10: **Loss of model-human similarity ($\Delta\rho/\rho_{all}$) due to energy constraints depends on the maximal energy gap and local excitatory connectivity.** Each point in the scatter plot represents the loss of model-human similarity due to the inability to cross the maximal energy gap given a specific combination of global coupling G, and local connectivity w_{EE} and w_{EI}. Overall, the loss increases with the gap size, which in turn depends on G (Figure 11a). The average loss (bars) decreases with increasing local excitatory connectivity (w_{EE}, w_{EI}). (*** p<0.001 with Tukey HSD; error bars are standard errors throughout the text)
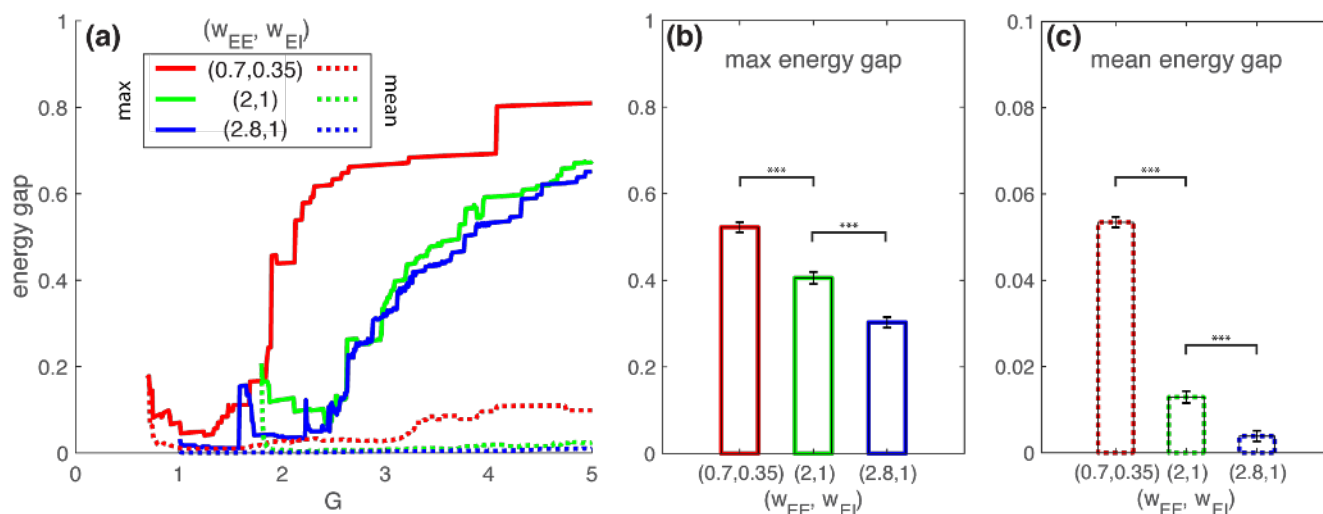

Figure 11: **Local (w_{EE}, w_{EI}) and global (G) structural connectivity jointly shape the energy cost of cross-attractor coordination.** (a) Overall, the maximal (solid lines) and average energy gaps (dashed lines) increase with global coupling G, though there is a transient decrease when maximal energy gap is less than 0.2. Both types of gaps decrease with increasing local connectivity w_{EE}, w_{EI} (b,c). (*** p<0.001 with Tukey HSD)

Is the energy demand for cross-attractor coordination uniform over the whole   456

21

brain? Here we compare the energy demand within the Default Model Network (DMN)—a signature of the resting brain—and other brain regions (Figure 12). Cross-attractor coordination is more energy demanding within DMN than the rest of the brain, measured by the ratio between the maximal energy gap within DMN v.s. others (gap ratio>1, above dashed line in Figure 12a; or equivalently log gap ratio>0 in Figure 12b). DMN dominates the energy consumption primarily when the overall energy consumption of the whole brain is low (max energy gap≤ 0.2, Figure 12b), and when local excitatory connections are stronger (left bars in Figure 12b).
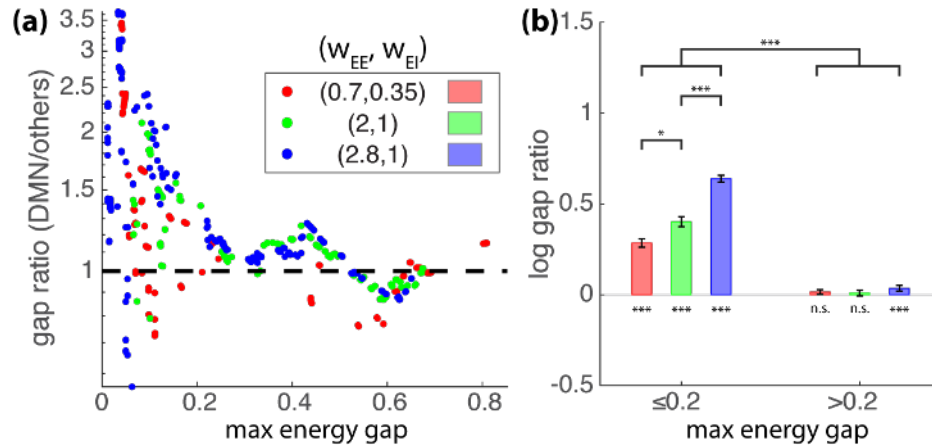

Figure 12: **Default Model Network (DMN) is more energy demanding than other networks.** DMN and other resting-state networks are defined based on the intersection between the present parcellation with Yeo et al's [77] 7 networks. (a) DMN generally contains a greater maximal energy gap than other networks (gap ratio>1), especially when the maximal energy gap of the whole brain (x-axis) is small (e.g. ≤ 0.2). (b) On average, the log gap ratio between DMN and other networks is significantly greater than zero (i.e. gap ratio>1) when the whole-brain maximal energy gap ≤ 0.2 (left three bars), but very close to zero when the whole-brain maximal energy gap > 0.2 (right three bars). The dominance of DMN's energy demand increases with local excitatory connectivity (left three bars: blue > green > red). (* $p<0.05$, *** $p<0.001$ with Tukey HSD)

3.4 Local and global causes of temporal diversity

Now we turn to the structural constraints on temporal diversity. In particular, we show how spectral properties of the simulated neural activities and corresponding hemodynamic responses are affected by both the diversity of local structural properties and the structure of the large-scale connectome.

Given a uniform global network, temporal diversity across the whole brain can be induced by the diversity of local excitatory-to-excitatory connection (w_{EE}), as shown in Figure 13a. Brain regions with relatively weak w_{EE} (blue) have low characteristic frequencies around 10 Hz (alpha range), while brain regions with strong w_{EE} (red) have higher characteristic frequencies around 30 Hz (beta/gamma range). In other words, the characteristic frequency of the oscillation increases monotonically with w_{EE} (see also Figure S4a). This is expected from the behavior of isolated brain regions (Figure 3d). In addition to the expected diversity, signs of coordination between regions can be seen as the wide-spread alpha peaks (Figure 13a). In contrast, regions with a higher characteristic frequency (beta/gamma range) are not as influential to other regions. That is, low-frequency oscillations, rather than high-frequency ones, are responsible for global coordination.

The above observations concern high-frequency dynamics typically measured

22

using, e.g. electroencephalography (EEG) and magnetoencephalography (MEG). For 483
low-frequency dynamics typical for functional magnetic resonance imaging (fMRI), 484
we examine the low-frequency content (0.01-0.1 Hz) of the normalized power spectra 485
of BOLD activities, derived from the same simulated neural dynamics (see Section S2 486
in Supplementary Materials for details). The result is shown in Figure 13b: there is 487
no significant dependency of low-frequency power on w_{EE} (Spearman correlation 488
$\rho = -0.029$, $p = 0.81$). In short, we find differential effects of local structural 489
diversity on neural dynamics at the time scales typical for different neural imaging 490
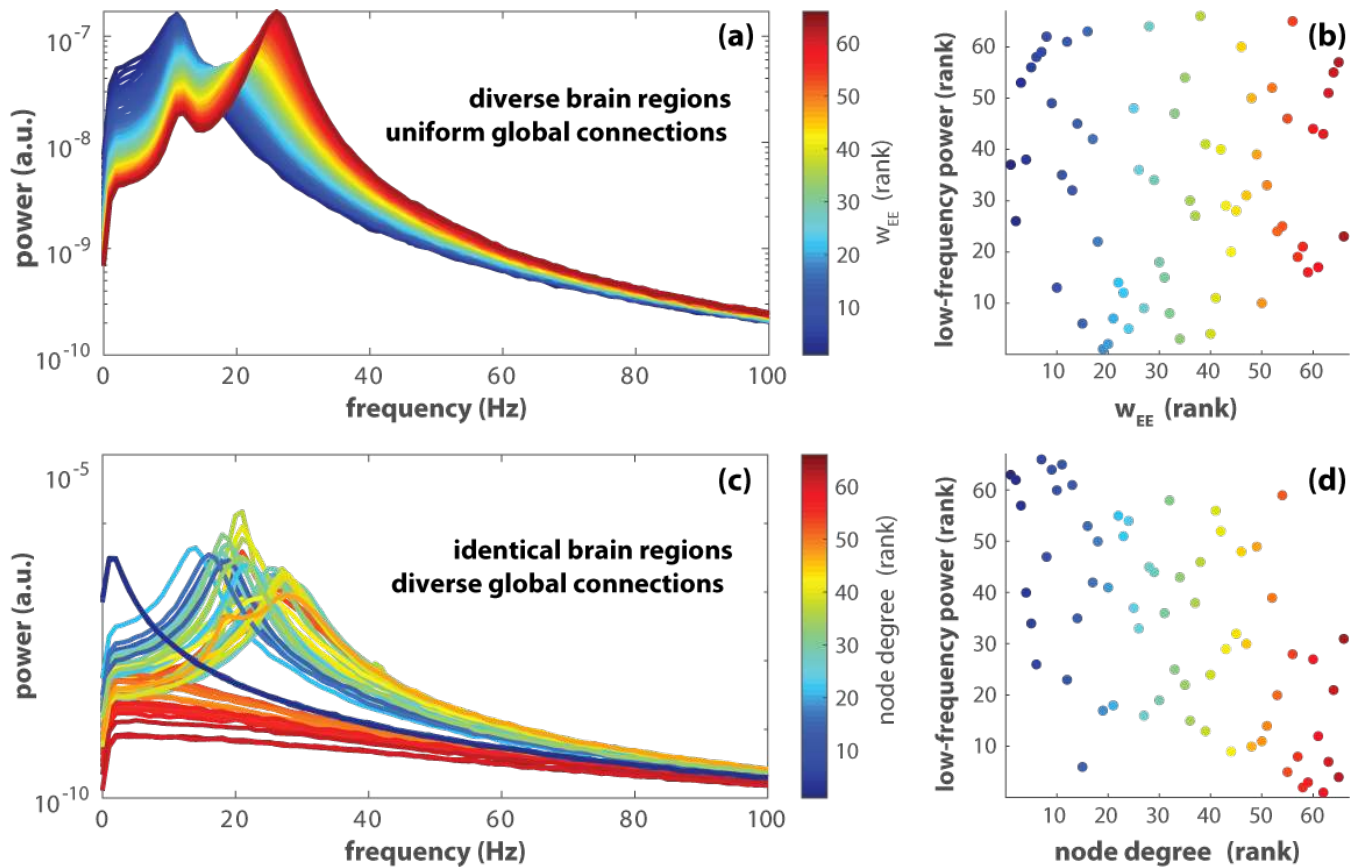modalities. 491

23

Figure 13: **Temporal diversity induced by diversity in local (a, b) and global structural connectivity (c, d).** Spectral analyses are based on two simulated trials of the global model (equation 4-6 with $N = 66$) each with identical initial conditions $S_E^{(i)}(0) = S_I^{(i)}(0) = 0.2$, a 1200s duration, and a moderate level of noise $\sigma = 0.01$. For the first simulated trial (a, b), different brain areas are endowed with different local connectivity, $w_{EE}^{(i)}$, evenly spread in the interval $[1, 2]$; the large-scale structural connectivity is set to be uniform, i.e. $C_{ij} = 1/(N-1)$, for $i \neq j$. In addition, the global coupling $G = 1.35$. (a) shows the power spectra of the excitatory gating variables $S_E^{(i)}$ for $i = 1, \cdots, N$. The spectrum for each brain region is color coded by the rank of w_{EE}—blue to red indicate the smallest to the largest w_{EE}. The peak frequency of these spectra clearly increases with w_{EE}. (b) shows the rank of the low-frequency power of the corresponding BOLD signal, integrated over the frequency range $[0.01, 0.1]$ Hz (see Section S2 for details), which depends little on the rank of w_{EE}. (c) and (d) show results of similar analyses but for the second simulated trial, where the individual brain regions are identical ($w_{EE}^{(i)} = 2$ for all i) but the global structural connectivity is realistic, i.e. C_{ij} here reflects the human connectome [59, 60] with the global coupling $G = 2.5$. Both low-frequency (d) and high-frequency (c) activities are highly affected by the degree of the brain region in the global network (rank color-coded).

On the other hand, temporal differentiation does not mandate the brain regions themselves to be structurally different. As shown in Figure 13c-d, locally identical brain regions can behave very differently due to the topology of the large-scale network (human connectome as in Section 3.3). The influence of large-scale structural connectivity on temporal diversity is manifested in both the high-frequency neural dynamics (Figure 13c; Figure S5a) and the low-frequency power of the BOLD signals (Figure 13d; Figure S5b). Specifically, the low-frequency power is inversely related

492
493
494
495
496
497
498

24

to the degree of each node (brain region) in the large-scale network (Spearman correlation $\rho = -0.584$, $p < 10^{-6}$). ₄₉₉ ₅₀₀

In Section S6, we demonstrate that the above effects are robust over 200 simulated trials of the same parameter settings. Overall, both local (Figure 13a,b; Figure S4) and large-scale structural connectivity (Figure 13c,d; Figure S5) contribute to the diversification of local dynamics. The contribution of local structural differences is stonger in a higher-frequency range (Figure 13d; Figure S4a), while the contribution of global structural connectivity is stronger in a very-low frequency range (Figure 13d; Figure S5b). Modeling real neural dynamics requires considering both sides of the spectrum.

4   Discussion

The present work shows systematically how multistability and temporal diversity of the brain can be shaped by structural constraints across scales using a biophysically constrained nonlinear dynamical model. We show that human-like functional connectivity emerges spontaneously from the multistable landscape as brain regions transition across attractors in a coordinated manner. The work suggests a *transition*-centered view of human functional connectivity, over a *attractor*-centered one. The theoretical and empirical implications are discussed below.

The rich dynamics of a single isolated brain region can be effectively controlled by two key local structural properties: local excitatory-to-excitatory connectivity (self-excitation) and local excitatory-to-inhibitory connectivity. In the real brain, local excitatory-to-excitatory connections are particularly abundant [78], and in our model, they contribute indispensably to multistability (Section S7). Multistability is a key source of biological complexity from molecular to social levels [30, 31], often tied to self-excitation or positive feedback [79–81]. The biophysical underpinnings of the present model links the mathematical prediction of multistability to physical manipulations. For example, varying the local connectivity in the model can be interpreted empirically as modulating the conductance of N-methyl-D-aspartate (NMDA) receptors in local neuronal populations, using pharmacological and endogenous antagonists and agonists such as ketamine [82] and dopamine [83]. Such manipulations have been theoretically predicted and shown to affect memory capacity [51, 52, 84].

At the large-scale network level, multistability can be created or amplified by the synergistic interaction between mono- or multi-stable brain regions (Section S7 Multistability). Different large-scale network structures have dramatically different capability at amplifying local complexity: a realistic global network (Figure 7 g-i) is much more powerful than a uniform one (Figure 7 d-f). The human connectome breaks the spatial symmetry of the global model, whereas symmetry breaking is often a key to complex dynamics [2, 38, 85–88]. The human connectome is also endowed with specific features such as modularity, small-worldness, and multiscale characteristics [1, 89–91]. A systematic study of how these features alter the geometry of the global dynamic landscape is worthy of further theoretical investigation (see Section S8).

Within the multistable landscape sculpted by the human connectome, coordination between model brain regions across different attractors gives rise to human-like functional connectivity (Figure 8b). Importantly, such cross-attractor coordination better captures human functional connectivity than within-attractor coordination— synchronization between brain regions near a single attractor (Figure 8c,d). This raises the possibility that functional connectivity patterns reflect transitions between stable brain states (Figure 6f) more than the brain states themselves (Figure 6d,e). This transition-centered view offers alternative perspectives on several theoretical and empirical issues. First, with a within-attractor approach [7], similar models exhibited much lower inter-hemispheric connectivity than that of humans. It was

25

attributed to an underestimation of structural connections across hemispheres [7, 9]. However, strong functional connectivity in humans is known to exist between regions that are not directly connected [92]. Thus, strong inter-hemispheric functional connectivity may reflect the nonlinearity in the dynamical system despite the weak structural connectivity. Cross-attractor approach takes into account such nonlinear effect. In contrast, within-attractor coordination can be approximated by a linear dynamical system, which closely depends on the structural connectivity [7, 8] (c.f. Figure 8d v.s. f). Second, cross-attractor coordination in the present study is measured over the entire dynamic landscape, which itself is time invariant. Empirically observed stability and convergence of human functional connectivity [93, 94] may reflect this invariance of the underlying landscape. The static landscape also support a dynamic view on functional connectivity [95], since at any given time the possible transitions depend on the current attractor (stable state). However, because transitions within two different sets of attractors may be similar, similar dynamic functional connectivity patterns, under a transition-centered view, may come from distinct places in the landscape. Thus, clustering of dynamic functional connectivity patterns may be difficult to interpret in dynamical system terms. Finally, although the pattern of cross-attractor coordination can remain similar as the landscape changes (Figure 9a-c), it is not the case for its energy cost (Figure 11). This means that the potential for exhibiting normal functional connectivity patterns may always be there, but different structural constraints impose different energy costs. In our model, the Default Mode Network dominates energy consumption over other parts of the brain when the energy gaps are overall small. This resonates with the empirical finding that aerobic glycolysis, accommodating small and rapid energy demands, is significantly elevated in the Default Mode Network [96].

The temporal diversity of the model brain is also affected by both local and global structural constraints. In the local model, oscillatory activity requires a sufficiently strong excitatory-to-inhibitory connection. The oscillation may be damped or sustained at various characteristic frequencies, contingent upon the strength of excitatory-to-excitatory connection (see Figure 3a-d and Section S7 Oscillation). The importance of inhibitory neurons and their interaction with pyramidal cells for generating rhythmic activity has been well demonstrated in both theoretical and empirical studies [97–101]. For multiple oscillatory processes to form complex spatiotemporal patterns, it often requires the coexistence of diverse time scales [31, 38, 102]. In the present model, temporal differentiation can be caused by local structural differences, i.e. the strength of local excitatory-to-excitatory connection (Figure 13ab). It has been shown that incorporating such local structural diversity in the reduced Wong-Wang model better describes real neural dynamics [9], demonstrating its empirical relevance. On the other hand, temporal differentiation can also be induced solely by the structure of the global network—the whole defining the parts (Figure 13cd). The diversity of node degree is a key contributor to the spectral diversity in the low-frequency range (Figure 13d), which has been observed empirically (e.g. [103]). It resonates with earlier findings that slow dynamics are more reflective of the large-scale network structure (e.g. [104]). These multiscale structural sources of temporal diversity may influence each other through their joint-action on brain synchronization and activity-based plasticity. Further theoretical investigation of such cross-scale interaction may shed light on how structural and dynamical properties stabilize each other across scales during brain development (see [105]).

In conclusion, complex dynamic features such as multistability and temporal diverse are both supported by local structural connectivity and further synergized by the structure of the large-scale network. Cross-attractor coordination between model brain regions in the multistable landscape provides a stronger explanation for human functional connectivity than within-attractor or near-equilibrium coordination. Energy costs of such coordination is further shaped by structural constraints across scales and prominent in the Default Mode Network. These findings suggest that

26

empirically observed resting functional connectivity reflects transitions more than stable brain states. Lowering the energy costs of such transitions may be a means to restore normal functional connectivity. Constrained by the biophysics, the modeling approach may be used to predict stimulation-induced transitions in experimental and clinical settings.

5   Acknowledgements

References

1. Sporns, O. & Tononi, G. Classes of network connectivity and dynamics. *Complexity* **7,** 28–38 (2001).

2. Kelso, J. A. S. *Dynamic Patterns: The Self-Organization of Brain and Behavior* (The MIT Press, Cambridge, Massachusetts, 1995).

3. Freeman, W. J. & Vitiello, G. Nonlinear brain dynamics as macroscopic manifestation of underlying many-body field dynamics. *Physics of Life Reviews* **3,** 93–118 (2006).

4. Bassett, D. S. & Siebenhühner, F. in *Multiscale Analysis and Nonlinear Dynamics* 179–204 (John Wiley & Sons, Ltd, 2013).

5. Deco, G., Jirsa, V. K. & McIntosh, A. R. Emerging concepts for the dynamical organization of resting-state activity in the brain. *Nature Reviews Neuroscience* **12,** 43 (2011).

6. Park, H.-J. & Friston, K. Structural and functional brain networks: from Connections to cognition. *Science* **342,** 1238411 (2013).

7. Deco, G. *et al.* Resting-state functional connectivity emerges from structurally and dynamically shaped slow linear fluctuations. *Journal of Neuroscience* **33,** 11239–11252 (2013).

8. Deco, G. *et al.* How local excitation–inhibition ratio impacts the whole brain dynamics. *Journal of Neuroscience* **34,** 7886–7898 (2014).

9. Demirtaş, M. *et al.* Hierarchical heterogeneity across human cortex shapes large-scale neural dynamics. *Neuron* **101,** 1181–1194.e13 (2019).

10. Golos, M., Jirsa, V. & Daucé, E. Multistability in large scale models of brain activity. *PLoS computational biology* **11,** e1004644 (2015).

11. Berger, H. Über das elektrenkephalogramm des menschen. *Archiv für Psychiatrie und Nervenkrankheiten* **87,** 527–570 (1929).

12. Bishop, G. H. Cyclic changes in excitability of the optic pathway of the rabbit. *American Journal of Physiology-Legacy Content* **103,** 213–224 (1932).

13. Raichle, M. E. & Mintun, M. A. Brain work and brain imaging. *Annual Review of Neuroscience* **29,** 449–476 (2006).

14. Fox, M. D., Snyder, A. Z., Zacks, J. M. & Raichle, M. E. Coherent spontaneous activity accounts for trial-to-trial variability in human evoked brain responses. *Nature Neuroscience* **9,** 23–25 (2006).

15. Schroeder, C. E. & Lakatos, P. Low-frequency neuronal oscillations as instruments of sensory selection. *Trends in Neurosciences* **32,** 9–18 (2009).

16. Liégeois, R. *et al.* Resting brain dynamics at different timescales capture distinct aspects of human behavior. *Nature Communications* **10,** 2317 (2019).

17. Zhang, D. & Raichle, M. E. Disease and the brain's dark energy. *Nature Reviews Neurology* **6,** 15–28 (2010).

18. Raichle, M. E. *et al.* A default mode of brain function. *Proceedings of the National Academy of Sciences* **98,** 676–682 (2001).

19. Greicius, M. D., Krasnow, B., Reiss, A. L. & Menon, V. Functional connectivity in the resting brain: a Network analysis of the default mode hypothesis. *Proceedings of the National Academy of Sciences* **100,** 253–258 (2002).

20. Fox, M. D. *et al.* The human brain is intrinsically organized into dynamic, anticorrelated functional networks. *Proceedings of the National Academy of Sciences* **102,** 9673–9678 (2005).

21. Damoiseaux, J. S. *et al.* Consistent resting-state networks across healthy subjects. *Proceedings of the National Academy of Sciences* **103,** 13848–13853 (2006).

22. Raichle, M. E. The restless brain. *Brain Connectivity* **1,** 3–12 (2011).

23. Hutchison, R. M., Womelsdorf, T., Gati, J. S., Everling, S. & Menon, R. S. Resting-state networks show dynamic functional connectivity in awake humans and anesthetized macaques. *Human Brain Mapping* **34,** 2154–77 (2012).

24. Hipp, J. F., Hawellek, D. J., Corbetta, M., Siegel, M. & Engel, A. K. Large-scale cortical correlation structure of spontaneous oscillatory activity. *Nature Neuroscience* **15,** 884–890 (2012).

25. Breakspear, M. Dynamic models of large-scale brain activity. *Nature Neuroscience* **20,** 340–352 (2017).

26. Deco, G., Jirsa, V. K. & McIntosh, A. R. Resting brains never rest: Computational insights into potential cognitive architectures. *Trends in Neurosciences* **36,** 268–274 (2013).

27. Stephan, K. E., Iglesias, S., Heinzle, J. & Diaconescu, A. O. Translational perspectives for computational neuroimaging. *Neuron* **87,** 716–732 (2015).

28. Kelso, J. A. S. Multistability and metastability: Understanding dynamic coordination in the brain. *Philosophical Transactions of the Royal Society B: Biological Sciences* **367,** 906–918 (2012).

29. Kuramoto, Y. *Chemical Oscillations, Waves, and Turbulence.* (Springer, Berlin, Heidelberg, 1984).

30. Laurent, M. & Kellershohn, N. Multistability: a Major means of differentiation and evolution in biological systems. *Trends in Biochemical Sciences* **24,** 418–422 (1999).

31. Zhang, M., Beetle, C., Kelso, J. A. S. & Tognoli, E. Connecting empirical phenomena and theoretical models of biological coordination across scales. *Journal of The Royal Society Interface* **16,** 20190360 (2019).

32. Buzsáki, G., Logothetis, N. & Singer, W. Scaling brain size, keeping timing: Evolutionary preservation of brain rhythms. *Neuron* **80,** 751–764 (2013).

33. Hopfield, J. J. Neural networks and physical systems with emergent collective computational abilities. *Proceedings of the National Academy of Sciences* **79,** 2554–2558 (1982).

34. Amit, D. J. & Brunel, N. Model of global spontaneous activity and local structured activity during delay periods in the cerebral cortex. *Cerebral Cortex* **7,** 237–252 (1997).

35. Hansen, E. C., Battaglia, D., Spiegler, A., Deco, G. & Jirsa, V. K. Functional connectivity dynamics: Modeling the switching behavior of the resting state. *NeuroImage* **105,** 525–535 (2015).

36. Buzsáki, G. & Draguhn, A. Neuronal oscillations in cortical networks. *Science* **304,** 1926–1929 (2004).

654
655
656
657
658
659
660
661
662
663
664
665
666
667
668
669
670
671
672
673
674
675
676
677
678
679
680
681
682
683
684
685
686
687
688
689
690
691
692
693
694
695
696
697
698
699
700
701
702

37. Buzsáki, G. & György, B. *Rhythms of the Brain* (Oxford University Press, New York, 2006).

38. Tognoli, E. & Kelso, J. A. S. The metastable brain. *Neuron* **81,** 35–48 (2014).

39. Uhlhaas, P. J. & Singer, W. Neuronal dynamics and neuropsychiatric disorders: Toward a translational paradigm for dysfunctional large-scale networks. *Neuron* **75,** 963–80 (2012).

40. Deco, G., Jirsa, V., McIntosh, A. R., Sporns, O. & Kötter, R. Key role of coupling, delay, and noise in resting brain fluctuations. *Proceedings of the National Academy of Sciences* **106,** 10302–10307 (2009).

41. Deco, G. & Jirsa, V. K. Ongoing cortical activity at rest: Criticality, multistability, and ghost attractors. *Journal of Neuroscience* **32,** 3366–3375 (2012).

42. Wilson, H. R. & Cowan, J. D. Excitatory and inhibitory interactions in localized populations of model neurons. *Biophysical Journal* **12,** 1–24 (1972).

43. Wilson, H. R. & Cowan, J. D. A mathematical theory of the functional dynamics of cortical and thalamic nervous tissue. *Kybernetik* **13,** 55–80 (1973).

44. Wong, K.-F. & Wang, X.-J. A recurrent network mechanism of time integration in perceptual decisions. *Journal of Neuroscience* **26,** 1314–1328 (2006).

45. Ermentrout, G. B. & Cowan, J. D. Temporal oscillations in neuronal nets. *Journal of Mathematical Biology* **7,** 265–280 (1979).

46. Campbell, S. & Wang, D. Synchronization and desynchronization in a network of locally coupled Wilson-Cowan oscillators. *IEEE Transactions on Neural Networks* **7,** 541–554 (1996).

47. Borisyuk, R. & Hoppensteadt, F. Oscillatory models of the hippocampus: a Study of spatio-temporal patterns of neural activity. *Biological Cybernetics* **81,** 359–371 (1999).

48. Frank, T., Daffertshofer, A., Peper, C., Beek, P. & Haken, H. Towards a comprehensive theory of brain activity: Coupled oscillator systems under external forces. *Physica D: Nonlinear Phenomena* **144,** 62–86 (2000).

49. Atasoy, S., Donnelly, I. & Pearson, J. Human brain networks function in connectome-specific harmonic waves. *Nature Communications* **7,** 10340 (2016).

50. Muldoon, S. F. *et al.* Stimulation-based control of dynamic brain networks. *PLOS Computational Biology* **12,** e1005076 (2016).

51. Anticevic, A. *et al.* NMDA receptor function in large-scale anticorrelated neural systems with implications for cognition and schizophrenia. *Proceedings of the National Academy of Sciences* **109,** 16720–5 (2012).

52. Murray, J. D. *et al.* Linking microcircuit dysfunction to cognitive impairment: Effects of disinhibition associated with schizophrenia in a cortical working memory model. *Cerebral Cortex* **24,** 859–872 (2014).

53. Brunel, N. & Sergi, S. Firing frequency of leaky intergrate-and-fire neurons with synaptic current dynamics. *Journal of Theoretical Biology* **195,** 87–95 (1998).

54. Wang, X.-J. Synaptic basis of cortical persistent activity: the Importance of NMDA receptors to working memory. *Journal of Neuroscience* **19,** 9587–9603 (1999).

55. Brunel, N. Dynamics of sparsely connected networks of excitatory and inhibitory spiking neurons. *Journal of Computational Neuroscience* **8,** 183–208 (2000).

56. Brunel, N. & Wang, X.-J. Effects of neuromodulation in a cortical network model of object working memory dominated by recurrent inhibition. *Journal of Computational Neuroscience* **11,** 63–85 (2001).

29

57. Wang, X.-J. Probabilistic decision making by slow reverberation in cortical circuits. *Neuron* **36,** 955–968 (2002).

58. Hagmann, P. *et al.* Mapping the structural core of human cerebral cortex. *PLoS Biology* **6,** e159 (2008).

59. Van Essen, D. C. *et al.* The WU-Minn Human Connectome Project: An overview. *NeuroImage* **80,** 62–79 (2013).

60. Civier, O., Smith, R. E., Yeh, C.-H., Connelly, A. & Calamante, F. Is removal of weak connections necessary for graph-theoretical analysis of dense weighted structural connectomes from diffusion MRI? *NeuroImage* (2019).

61. Yeomans, J. S. The absolute refractory periods of self-stimulation neurons. *Physiology & Behavior* **22,** 911–919 (1979).

62. Andersen, P., Silfvenius, H., Sundberg, S. & O. Sveen, H. W. Functional characteristics of unmyelinated fibres in the hippocampal cortex. *Brain Research* **144,** 11–18 (1978).

63. Abbott, L. F. & Chance, F. S. Drivers and modulators from push-pull and balanced synaptic input. *Progress in Brain Research* **149,** 147–155 (2005).

64. Renart, A., Brunel, N. & Wang, X.-J. in *Computational Neuroscience: A Comprehensive Approach* (ed Feng, J.) 432–490 (CRC Press, 2003).

65. Desikan, R. S. *et al.* An automated labeling system for subdividing the human cerebral cortex on MRI scans into gyral based regions of interest. *NeuroImage* **31,** 968–980 (2006).

66. Tournier, J.-D., Calamante, F. & Connelly, A. *Improved probabilistic streamlines tractography by 2 order integration over fibre orientation distributions* in *Proceedings of the 18th Annual Meeting of ISMRM (International Society for Magnetic Resonance in Medicine)* (2010), 1670.

67. Smith, R. E., Tournier, J.-D., Calamante, F. & Connelly, A. Anatomically-constrained tractography: Improved diffusion MRI streamlines tractography through effective use of anatomical information. *NeuroImage* **62,** 1924–1938 (2012).

68. Smith, R. E., Tournier, J.-D., Calamante, F. & Connelly, A. SIFT2: Enabling dense quantitative assessment of brain white matter connectivity using streamlines tractography. *NeuroImage* **119,** 338–351 (2015).

69. Esteban, O. *et al.* fMRIPrep: a robust preprocessing pipeline for functional MRI. *Nature Methods* (2018).

70. Esteban, O. *et al.* fMRIPrep. *Software* (2018).

71. Gorgolewski, K. *et al.* Nipype: a flexible, lightweight and extensible neuroimaging data processing framework in Python. *Frontiers in Neuroinformatics* **5,** 13 (2011).

72. Gorgolewski, K. J. *et al.* Nipype. *Software* (2018).

73. Cox, R. W. & Hyde, J. S. Software tools for analysis and visualization of fMRI data. *NMR in Biomedicine* **10,** 171–178 (1997).

74. Greve, D. N. & Fischl, B. Accurate and robust brain image alignment using boundary-based registration. *NeuroImage* **48,** 63–72 (2009).

75. Jenkinson, M., Bannister, P., Brady, M. & Smith, S. Improved Optimization for the Robust and Accurate Linear Registration and Motion Correction of Brain Images. *NeuroImage* **17,** 825–841 (2002).

76. Power, J. D. *et al.* Methods to detect, characterize, and remove motion artifact in resting state fMRI. *NeuroImage* **84,** 320–341 (2014).

77. Yeo, B. T. T. *et al.* The organization of the human cerebral cortex estimated by intrinsic functional connectivity. *Journal of Neurophysiology* **106,** 1125–1165 (2011).

78. Somogyi, P., Tamás, G., Lujan, R. & Buhl, E. H. Salient features of synaptic organisation in the cerebral cortex. *Brain Research Reviews* **26,** 113–135 (1998).

79. Attneave, F. Multistability in perception. *Scientific American* **225,** 62–71 (1971).

80. Arthur, W. B. Positive feedbacks in the economy. *Scientific American* **262,** 92–99 (1990).

81. Angeli, D., Ferrell, J. E. & Sontag, E. D. Detection of multistability, bifurcations, and hysteresis in a large class of biological positive-feedback systems. *Proceedings of the National Academy of Sciences* **101,** 1822–1827 (2004).

82. Orser, B. A., Pennefather, P. S. & MacDonald, J. F. Multiple mechanisms of ketamine blockade of N-methyl-D-aspartate receptors. *Anesthesiology* **86,** 903–917 (1997).

83. Wang, M., Wong, A. H. & Liu, F. Interactions between NMDA and dopamine receptors: a Potential therapeutic target. *Brain research* **1476,** 154–63 (2012).

84. Verma, A. & Moghaddam, B. NMDA receptor antagonists impair prefrontal cortex function as assessed via spatial delayed alternation performance in rats: Modulation by dopamine. *Journal of Neuroscience* **16,** 373–379 (1996).

85. Golubitsky, M., Stewart, I., Buono, P.-L. & Collins, J. J. Symmetry in locomotor central pattern generators and animal gaits. *Nature* **401,** 693–695 (1999).

86. Golubitsky, M. & Stewart, I. *The Symmetry Perspective - From Equilibrium to Chaos in Phase Space and Physical Space* (Birkhäuser, Basel, 2002).

87. Kelso, J. A. S., Dumas, G. & Tognoli, E. Outline of a general theory of behavior and brain coordination. *Neural Networks* **37,** 120–131 (2013).

88. Pillai, A. S. & Jirsa, V. K. Symmetry breaking in space-time hierarchies shapes brain dynamics and behavior. *Neuron* **94,** 1010–1026 (2017).

89. Sporns, O. Network analysis, complexity, and brain function. *Complexity* **8,** 56–60 (2002).

90. Sporns, O. in *Coordination Dynamics: Issues and Trends* (eds Jirsa, V. K. & Kelso, J. A. S.) 197–215 (Springer Berlin Heidelberg, Berlin, Heidelberg, 2004).

91. Sporns, O. The human connectome: a Complex network. *Annals of the New York Academy of Sciences* **1224,** 109–125 (2011).

92. Honey, C. J. *et al.* Predicting human resting-state functional connectivity from structural connectivity. *Proceedings of the National Academy of Sciences* **106,** 2035–2040 (2009).

93. Laumann, T. O. *et al.* On the Stability of BOLD fMRI Correlations. *Cerebral Cortex* **27,** 4719–4732 (2016).

94. Gordon, E. M. *et al.* Precision Functional Mapping of Individual Human Brains. *Neuron* **95,** 791–807.e7 (2017).

95. Hutchison, R. M. *et al.* Dynamic functional connectivity: Promise, issues, and interpretations. *NeuroImage* **80,** 360–378 (2013).

96. Vaishnavi, S. N. *et al.* Regional aerobic glycolysis in the human brain. *Proceedings of the National Academy of Sciences* **107,** 17757–17762 (2010).

31

97. Wang, X.-J. & Buzsáki, G. Gamma oscillation by synaptic inhibition in a hippocampal interneuronal network model. *Journal of Neuroscience* **16,** 6402–6413 (1996).

98. Bartos, M., Vida, I. & Jonas, P. Synaptic mechanisms of synchronized gamma oscillations in inhibitory interneuron networks. *Nature Reviews Neuroscience* **8,** 45–56 (2007).

99. Middleton, S. *et al.* NMDA receptor-dependent switching between different gamma rhythm-generating microcircuits in entorhinal cortex. *Proceedings of the National Academy of Sciences* **105,** 18572–7 (2008).

100. Atallah, B. V. & Scanziani, M. Instantaneous modulation of gamma oscillation frequency by balancing excitation with inhibition. *Neuron* **62,** 566–577 (2009).

101. Mann, E. O. & Mody, I. Control of hippocampal gamma oscillation frequency by tonic inhibition and excitation of interneurons. *Nature Neuroscience* **13,** 205–212 (2009).

102. Zhang, M., Kalies, W. D., Kelso, J. A. S. & Tognoli, E. Topological portraits of multiscale coordination dynamics. *Journal of Neuroscience Methods* **339,** 108672 (2020).

103. Baria, A. *et al.* Linking human brain local activity fluctuations to structural and functional network architectures. *NeuroImage* **73,** 144–155 (2013).

104. Honey, C. J., Kötter, R., Breakspear, M. & Sporns, O. Network structure of cerebral cortex shapes functional connectivity on multiple time scales. *Proceedings of the National Academy of Sciences* **104,** 10240–10245 (2007).

105. Uddin, L. Q., Supekar, K. S., Ryali, S. & Menon, V. Dynamic reconfiguration of structural and functional connectivity across core neurocognitive brain networks with development. *Journal of Neuroscience* **31,** 18578–18589 (2011).

849
850
851
852
853
854
855
856
857
858
859
860
861
862
863
864
865
866
867
868
869
870
871
872
873

Supplementary Materials

S1 Computation of bifurcation diagrams

The computation of bifurcation diagrams (Figure 7) was carried out in MATLAB, utilizing the build-in function `fsolve`. Given a proper initial guess, `fsolve` provides the coordinates of a nearby fixed point and the Jacobian matrix at the fixed point. The spectrum $\{\lambda_k\}_{k=1}^{2N}$ of the Jacobian matrix is used to classify the fixed point, where N is the number of brain regions in the model. The fixed point is a stable equilibrium if λ_k is real and negative for all k. The fixed point is associated with damped oscillation if $\operatorname{Re}\lambda_k < 0$ for all k and $\operatorname{Im}\lambda_k \neq 0$ for some k. The fixed point is associated with a limit cycle if $\operatorname{Re}\lambda_k > 0$ and $\operatorname{Im}\lambda_k \neq 0$ for some k with the additional criteria that after a small perturbation from the fixed point, the time-average of the solution remains close to the fixed point. All other types of fixed points are classified as unstable. For damped oscillation and limit cycles in the local model, the frequency of the oscillation (Figure 3) is defined as $|\operatorname{Im}\lambda_k|/(2\pi)$.

For the local model, a 2D dynamical system, the complete characterization of all fixed points is relatively easy by searching exhaustively through a grid of initial guesses (as for Figure 7a-c). This approach becomes unfeasible when it comes to the global model due to the high dimensionality. Thus, for the global model, we implemented a recursive search: for each value of G, (1) find zeros of equation 4-6 (main text) given a set of initial guesses that includes, if any, the zeros for $G - \delta G$ ($\delta G = 0.01$ for the present study); (2) sort the list of zeros obtained from (1) by the average of $S_E^{(i)}$'s; (3) use the middle points between consecutive zeros in the sorted list as initial guesses; (4) continue to use middle points between past initial guesses as new initial guesses recursively until at least one new zero is found or the recursion has reached a certain depth; (5) append the new zero(s) to the list of zeros and repeat (2)-(5) until the number of identified zeros exceeds a certain value. In the present study, we limit the maximal depth in (4) to 8 and the maximal number of zeros in (5) to 200.

S2 Computation of BOLD signal and low-frequency power

In the present study, we are interested in not only the high-frequency activity measurable by, for example, EEG recordings but also low-frequency fluctuations that are often a subject of investigation in fMRI studies. Therefore, we simulated the BOLD activities induced by the underlying neural dynamics and examine their low-frequency properties.

BOLD (Blood-oxygen-level-dependent) activities are computed using the Balloon-Windkessel model [1–4]. The hemodynamic response of the ith brain area takes the form

$$\dot{s}_i = z_i - \kappa_i s_i - \gamma_i(f_i - 1) \tag{S1}$$

$$\dot{f}_i = s_i \tag{S2}$$

$$\tau_i \dot{v}_i = f_i - v_i^{1/\alpha} \tag{S3}$$

$$\tau_i \dot{q}_i = \frac{f_i}{\rho_i}[1 - (1-\rho_i)^{1/f_i}] - v_i^{1/\alpha-1}q_i \tag{S4}$$

$$BOLD_i = V_0[k_1(1-q_i) + k_2(1-q_i/v_i) + k_3(1-v_i)] \tag{S5}$$

where the interpretation and value of the parameters are given in Table S1. The initial condition is

$$[s_i(0), f_i(0), v_i(0), q_i(0)] = [0, 1, 1, 1] \tag{S6}$$

which is a hemodynamic equilibrium state without neural activity. $z_i(t)$ is the simulated neural activity, corresponding to the gating variable of the excitatory populations $S_E^{(i)}(t)$.

33

parameter	interpretation	value
z_i	neuronal activity	$S_E^{(i)}$
s_i	vasodilatory signal	variable
f_i	blood inflow	variable
v_i	blood volume	variable
q_i	deoxyhemoglobin content	variable
κ_i	rate of signal decay	$0.65(s^{-1})$
γ_i	rate of flow-dependent elimination	$0.41(s^{-1})$
τ_i	hemodynamic transit time	0.98 (s)
α	Grubb's exponent	0.32
ρ	resting oxygen extraction fraction	0.34
V_0	resting blood volume fraction	0.02
k_1	BOLD weight parameter	$7\rho_i$
k_2	BOLD weight parameter	2
k_3	BOLD weight parameter	$2\rho_i - 0.2$

Table S1: Parameters of the Balloon-Windkessel model of BOLD activities, obtained from [4].

The power spectrum for each simulated BOLD time series is computed using Welch's method [5], after being subsampled at 720ms intervals (matching the TR of resting state fMRI used in the Human Connectome Project [6]). The full power spectrum $P(\omega)$ was first normalized such that

$$\int_0^{\omega_N} P(\omega)\, \mathrm{d}\omega = 1 \tag{S7}$$

where ω_N is the Nyquist frequency (approximately 0.7 Hz for the chosen sampling interval). The low-frequency power is defined as

$$p_\ell = \int_{0.01}^{0.1} P(\omega)\, \mathrm{d}\omega. \tag{S8}$$

S3 Discretization of regional states

Although the dynamic landscape of the global model can be quite complex (Figure 7g-i), each region in the globally connected network still falls into discrete states (Figure S1) very much like in the local model (disconnected stripes in Figure 7a-c)—it is the combination of regional states that produces a great variety of attractors at the global level. Discretized regional states (number on black disks in Figure S1) thus give rise to discretized attractors in the global model. Rank correlation (Spearman) between regional states across these discretized attractors are used to quantify *cross-attractor coordination* in the model brain (Figure 8b in the main text). Using discretized attractors, we quantify how much two regions move up and down together across attractors without considering the distance between the attractors. The distance between attractors are considered separately as the energy cost that constrains such transitions (Figure 11 in the main text).
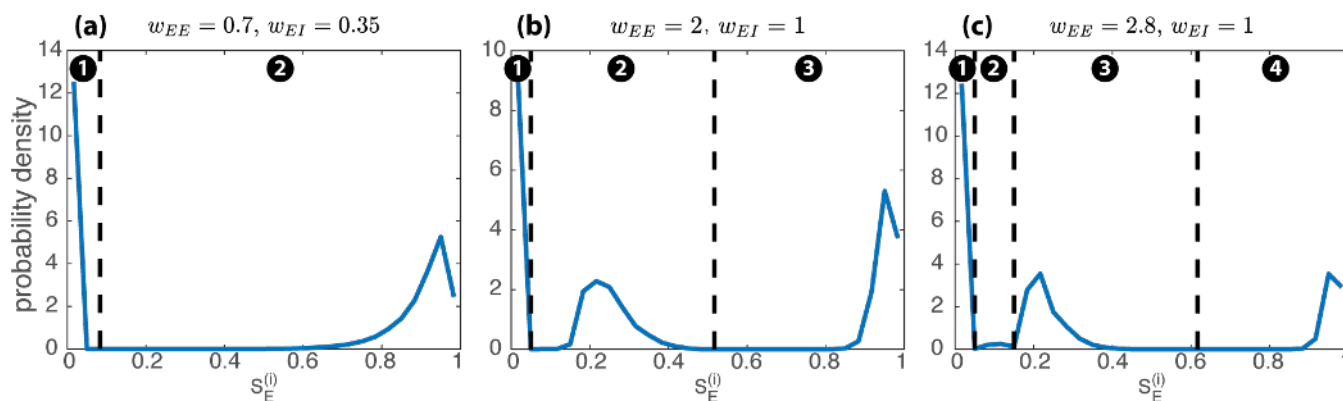
34

Figure S1: **Brain regions fall into discrete states in the global model**. Blue curves in (a-c) show the distribution of the state of individual brain regions ($S_E^{(i)}$ for any i) in the attractors in the bifurcation diagrams (Figure 7g-i) respectively. Black dashed lines indicate the location of local minima in the distributions. These minima are used to discretize the continuous variable $S_E^{(i)}$ into integer-indexed (discrete) states (number in black disks).

S4 Reliability of the average functional connectivity

The average functional connectivity is highly similar between Day 1 (Figure 8a in the main text) and Day 2 (Figure S2a). Linear regression analysis indicates that the Day-1 matrix is highly predictive of the Day-2 matrix (red x in Figure S2b; $\beta_1 = 0.98$, t(2143)=203, p<0.001, $R^2 = 0.951$; only elements below the diagonal are compared due to the symmetry of the matrix). Moreover, the functional connectivity matrix (Figure 8a in the main text) obtained using Spearman correlation is highly predictive of the corresponding Pearson correlation coefficients (Figure S2c; $\beta_1 = 1.03$, t(2143)=897, p<0.001, $R^2 = 0.997$), which itself is highly consistent across two days (blue o in S2b; $\beta_1 = 0.97$, t(2143)=211, p<0.001, $R^2 = 0.954$).
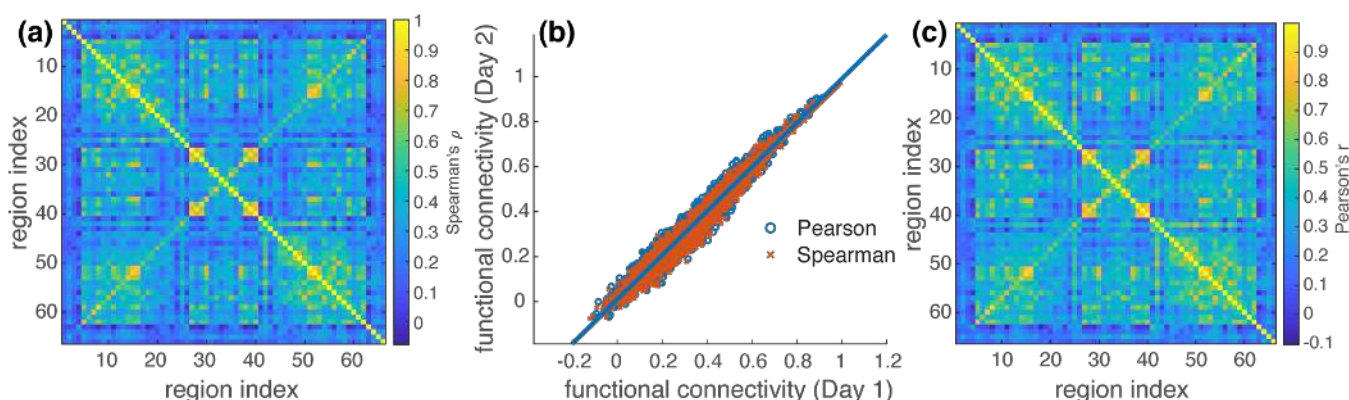

Figure S2: **Average human functional connectivity highly reliable across two days and the types of correlation analysis**. (a) shows the functional connectivity averaged across the same subjects as in Figure 8a (main text) but using the resting fMRI data (two runs) from Day 2. The matrices from the two days are highly correlated (b; red x). (c) shows the functional connectivity estimated using Pearson correlation averaged over all runs in Day 1, which is also consistent across two days (b; blue o), and is not markedly different from Figure 8a (main text). See text for statistical information.

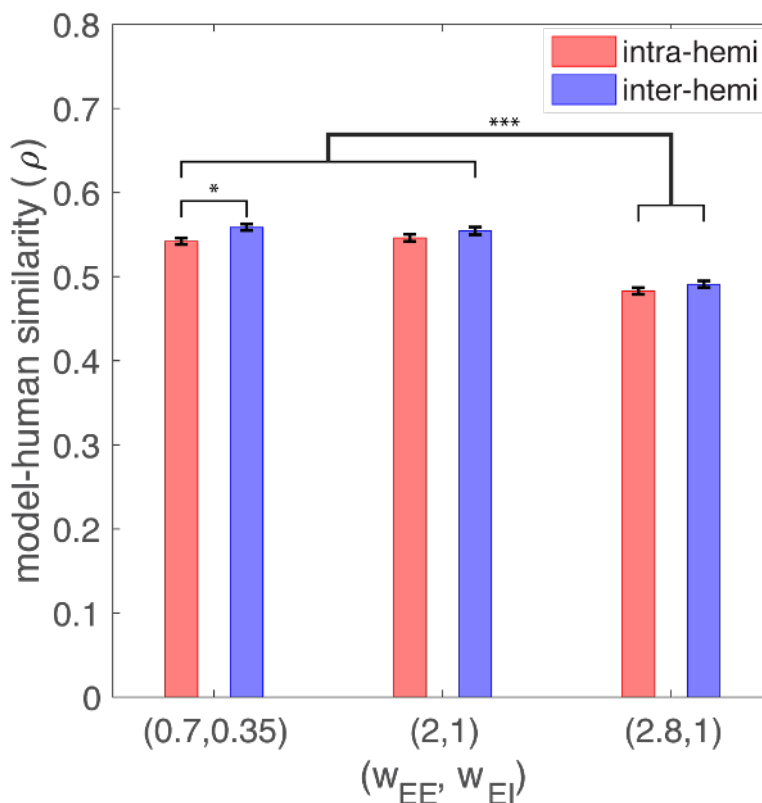## S5   Mean comparisons of human-model similarity

Figure S3: **Average effects of local structural connectivity on model-human similarity**. Cross-attractor coordination in the model well captures human functional connectivity for both intra- (red) and inter-hemispheric interaction (blue). The model-human correlation (Spearman's ρ) is slightly worse when local excitatory connection is too strong ($w_{EE} = 2.8$, $w_{EI} = 1$). (* p<0.05, *** p<0.001, with Tukey HSD)

S6   Dependency of spectral properties on local and global structural connectivity

In Figure 13 of the main text, we illustrate with two simulated trials how high-frequency and low-frequency dynamics depend on local excitatory-to-excitatory connectivity w_{EE} and the topology of the global network. To show that these effects are not incidental, we simulated 200 trials for each of the conditions: (1) the global network is uniform but local connectivity w_{EE} is diverse (as in Figure 13a,b), and (2) local connectivity w_{EE} is identical but the global network follows the human connectome (as in Figure 13c,d). We characterize the high-frequency content of a spectrum as its peak frequency, i.e. the frequency at which the spectral power is the highest (e.g. peaks in Figure 13a,c); the low-frequency content as the integral of the power between 0.01 and 0.1 Hz (Section S2). The dependency of these features on local (w_{EE}) and global structural properties (node degree) is quantified using Spearman correlation. The distributions of the correlation coefficients (ρ) and corresponding p-values are shown in Figure S4 and Figure S5 for condition 1 and 2 respectively. Figure S4 shows that local structural connectivity w_{EE} strongly affects the peak frequency of the brain region (a,c) but not so much the low-frequency power (b,d). The stronger the local connectivity, the higher the peak frequency. Figure S5 shows that the node degree of the global network has a strong and negative effect

on the low-frequency power, and a weak and positive effect on the peak frequency. Figure 13 illustrates such dependencies using typical trials (median correlation coefficients) from the distributions (Figure S4-S5).

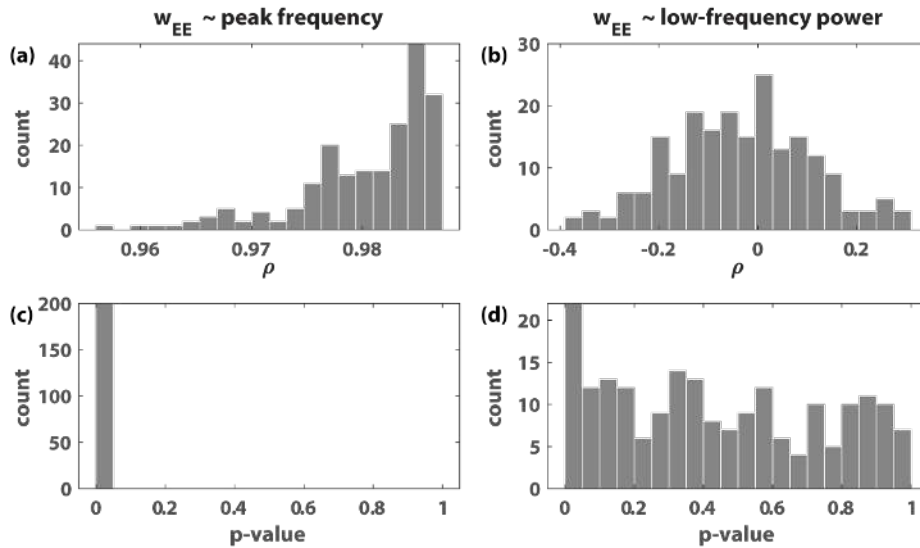<div style="text-align:right">956
957
958</div>

Figure S4: **Dependency of peak frequency and low-frequency power on local excitatory-to-excitatory connectivity**. 200 trials are simulated following the same parameter setting as Figure 13a,b, where the global network is uniform but the local connectivity w_{EE}'s spread between 1 to 2 for different brain regions. The noise terms in equation 4-5 make these trials different realizations of the same noisy process. The peak frequency of the spectra, e.g. from 10 to 30 Hz in Figure 13a, strongly depends on local connectivity w_{EE} (a: ρ's all close to 1; c: p-values all less than 0.05). In contrast, low-frequency power does not significantly depend on w_{EE} (b: ρ's distribute around zero; d: p-values spread between 0 and 1). Figure 13b shows this lack of dependency in an example trial that corresponds to the median of the distribution (b).
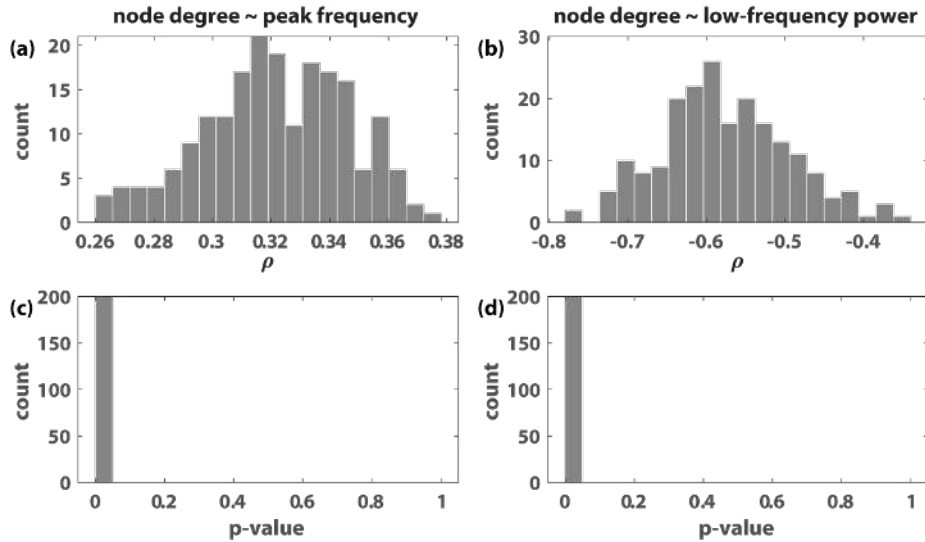
Figure S5: **Dependency of peak frequency and low-frequency power on node degree in the global network**. 200 trials are simulated following the same parameter setting as Figure 13c,d, where the local connectivity w_{EE}'s are the same across brain regions but the global-network reflects the human connectome (see main text). The peak frequency of the spectra, e.g. between 0 and 30 Hz in Figure 13c, moderately increases with the node degree of each region (a: positive ρ's around 0.32; c: p-values all less than 0.05). Low-frequency power decreases more significantly with node degree (b: ρ's distribute around -0.6; d: p-values all less than 0.05). Figure 13d illustrates this dependency with an example trial that corresponds to the median of the distribution (b).

S7 Analysis of the local model

We can see from the numerical analysis that the nullclines (dashed lines in Figure 4) crucially constraint the dynamics of the local model (equation 1-3). Here we take a closer look at their shapes. Red nullcline indicates where there is only vertical flow,

$$\frac{\mathrm{d}\,S_E}{\mathrm{d}\,t} = 0$$

$$\Rightarrow -\frac{S_E}{\tau_E} + (1 - S_E)\gamma_E\,H_E(w_{EE}S_E - w_{IE}S_I + I_E) = 0$$

$$\Rightarrow S_I = f(S_E) = \frac{w_{EE}}{w_{IE}}S_E - \frac{1}{w_{IE}}H_E^{-1}\left(\frac{S_E}{\tau_E\gamma_E(1 - S_E)}\right) + \frac{I_E}{w_{IE}}, \qquad \text{(S9)}$$

and blue nullcline indicates where there is only horizontal flow,

$$\frac{\mathrm{d}\,S_I}{\mathrm{d}\,t} = 0$$

$$\Rightarrow -\frac{S_I}{\tau_I} + (1 - S_I)\gamma_I\,H_I(w_{EI}S_E - w_{II}S_I + I_I) = 0$$

$$\Rightarrow S_E = g(S_I) = \frac{w_{II}}{w_{EI}}S_I + \frac{1}{w_{EI}}H_I^{-1}\left(\frac{S_I}{\tau_I\gamma_I(1 - S_I)}\right) - \frac{I_I}{w_{EI}}. \qquad \text{(S10)}$$

What is common between the two nullcines, $S_I = f(S_E)$ and $S_E = g(S_I)$, is that their shape crucially depends on a linear term S_p and the inverse of the transfer function H_p^{-1} for $p \in \{E, I\}$. Both terms are monotonically increasing with S_p ($H_p^{-1}(\bullet)$ and $S_p/(1 - S_p)$ are both monotonically increasing function; so is their composition). H_p^{-1} is only defined on a domain between 0 and r_{max}, for which the

nullclines are confined within the interval

$$\left[0, 1 - \frac{1}{r_{max}\tau_p\gamma_p}\right]. \tag{S11}$$

Within this interval $S_I = f(S_E)$ (equation S9; red nullcline), overall, goes down from $+\infty$ to $-\infty$, while $S_E = g(S_I)$ (equation S10; blue nullcline) goes up from $-\infty$ to $+\infty$. This results from the dominant effect of H_p^{-1} for a very large or very small input.

In between these extremes, the effect of the linear term is more pronounced. This is especially the case for $S_I = f(S_E)$ (red nullcline): the linear term monotonically increases with S_E, counteracting the descending trend of $-H_E^{-1}$. Given a sufficiently strong excitatory-to-excitatory connection w_{EE} (self-excitation), the linear term "twists" the nullcline counterclockwise, creating an ascending branch in the middle. If we balance the level of self-excitation with inhibitory-feedback—let $w_{EE} = w_{IE}$—equation S9 becomes

$$S_I = f(S_E) = S_E - \frac{1}{w_{EE}}H_E^{-1}\left(\frac{S_E}{\tau_E\gamma_E(1-S_E)}\right) + \frac{I_E}{w_{EE}}. \tag{S12}$$

In this simplified case, increasing self-excitation w_{EE} reduces the influence of H_E^{-1} such that the slope of middle branch approaches 1.

For $S_E = g(S_I)$ (equation S10), the linear term and the H_I^{-1} term increase together, so that $S_E = g(S_I)$ (blue nullcline) is always monotonically increasing. Given a fixed w_{II}, $S_E = g(S_I)$ increases with S_I at an overall slower rate for larger w_{EI}, or more conveniently seen as $S_I = g^{-1}(S_E)$ increasing faster with S_E for larger w_{EI}. Intuitively, increasing w_{EI} twists $S_E = g(S_I)$ counterclockwise, seen as the middle segment of the blue nullcline becoming more vertical.

We have discussed above how local connectivity w_{EE} and w_{EI} influence the gross geometry of the nullclines—twisting the middle segment of the curve counterclockwise. But how are these geometric changes going to affect the dynamics? We show below that they critically control the multistability and oscillation in the local model.

Multistability. For the local model to be multistable, $S_I = f(S_E)$ (red nullcline) must have an ascending branch, i.e. $f(S_E)$ cannot be monotonically decreasing.

Proof. Suppose that $f(x)$ and $g^{-1}(x)$ are monotonic functions for $x \in [0,1]$. Specially, $g^{-1}(x)$ is monotonically increasing; $f(x)$ is monotonically decreasing. Assume that $f(x)$ and $g^{-1}(x)$ intersect at two points $x_1 \leqslant x_2$, i.e. $f(x_1) = g^{-1}(x_1)$ and $f(x_2) = g^{-1}(x_2)$. Since $g^{-1}(x)$ is monotonically increasing, we have $g^{-1}(x_1) \leqslant g^{-1}(x_2)$, which implies $f(x_1) \leqslant f(x_2)$. Meanwhile, since $f(x)$ is monotonically decreasing, $f(x_1) \geqslant f(x_2)$. Thus, we have $f(x_1) = f(x_2)$, and by monotonicity, $x_1 = x_2$. In other words, if the two functions intersect, there must be a unique intersection.

Since $g^{-1}(x)$ is always monotonically increasing and the existence of multistability requires the existence of multiple intersections between $g^{-1}(x)$ and $f(x)$, a monotonically decreasing $f(x)$ implies that the system cannot be multistable. In other words, if the system is multistable, then $f(x)$ cannot be monotonically decreasing. $\square$

This result highlights the importance of self-excitation w_{EE} in equation S9 and equation S12—multistability can only occur when w_{EE} is sufficiently large. Correspondingly in the numerical result (Figure 3), the region of multistability appears only for larger w_{EE}'s.

Note that the above argument is not restricted to the present model, but applicable to models that share the geometry form of the Wilson-Cowan model in general. Nevertheless, one would hope to know how large a w_{EE} is large enough for multistability to be possible, and this depends on the specific formulation of the transfer function (equation 3) and the underlying assumptions about neuronal level properties

39

(equation 15). Ideally, to know the minimal w_{EE}, one need to find the minimal slope of $H_E^{-1}(u(S_E))$ with respective to S_E, where $u(S_E) := S_E/(\tau_E \gamma_E(1 - S_E))$. The exact solution is, however, rather perplexing to calculate. Here we provide a rough, but simple, estimation instead. The slope of interest is

$$\frac{\mathrm{d}}{\mathrm{d}\,S_E} H_E^{-1}(u(S_E)) = \frac{\mathrm{d}\,H_E^{-1}(u)}{\mathrm{d}\,u} \frac{\mathrm{d}\,u}{\mathrm{d}\,S_E} \tag{S13}$$

$$= \frac{\left(H_E^{-1}\right)'(u)}{\tau_E \gamma_E(1 - S_E)^2}. \tag{S14}$$

Instead of finding the minimum of equation S14, we aim to find a representative point S_E^* such that equation S14 is relatively small.

One option is to use the minimum of the numerator. The minimum of the numerator $\left(H_E^{-1}\right)'(u)$ is simply the reciprocal of the maximum of $H_E'(v)$, where $v = H_E^{-1}(u)$. By design, H_E reaches its maximal slope a_E at the inflection point $\hat{x}$, where $H_E(v) = r_{max}/2$. That is, we need

$$\frac{S_E^*}{\tau_E \gamma_E(1 - S_E^*)} = \frac{r_{max}}{2}$$

$$S_E^* = \frac{1}{2\, r_{max}^{-1} \tau_E^{-1} \gamma_E^{-1} + 1}.$$

But note here that, in the case where r_{max} is a large number, the representative point S_E^* is very close to one, which further results in a small denominator in equation S14 and a large slope for H_E^{-1}. Thus, the inflection point of $H_E(v)$ is not a very good choice.

To avoid the small denominator problem for equation S14, we need to choose a S_E^* as small as possible while $H_E(v)$ remains close to the line $a_E v - b_E$. For this purpose, we take v^* to be the intersection between the line $a_E v - b_E$ and the horizontal axis,

$$a_E v^* - b_E = 0$$

$$\Rightarrow v^* = \frac{b_E}{a_E}$$

$$\Rightarrow H_E(v^*) \approx \frac{1}{d_E}, \quad H_E'(v^*) \approx \frac{a_E}{2} \tag{S15}$$

(approximate values can be obtained from the Taylor expansion of $\hat{H}_E$ near v^*). Given equation S15, we need

$$\frac{S_E^*}{\tau_E \gamma_E(1 - S_E^*)} = \frac{1}{d_E} \tag{S16}$$

$$\Rightarrow S_E^* = \frac{1}{d_E \tau_E^{-1} \gamma_E^{-1} + 1} \tag{S17}$$

and

$$\frac{\mathrm{d}\,H_E^{-1}(u(S_E))}{\mathrm{d}\,S_E}\bigg|_{S_E=S_E^*} = \frac{2}{a_E \tau_E \gamma_E(1 - S_E^*)^2}$$

$$= \frac{2(1 + d_E^{-1}\tau_E \gamma_E)^2}{a_E \tau_E \gamma_E} =: h_E. \tag{S18}$$

Now for the nullcline $S_I = f(S_E)$ to have a positive slope at S_E^*, one simply needs

$$w_{EE} > h_E. \tag{S19}$$

Here h_E is approximately 0.2 based on the present parameter choices, inherited from Wong and Wang's initial derivation [7]. This result is confirmed numerically by the bifurcation diagrams (Figure 7a-c vs. Figure S6a) of the local model—multistability exists for some level of input I_E when $w_{EE} > 0.2$.

Oscillation. Now we look for the conditions for oscillation to emerge. Here we are mainly concerned with the oscillation occurring on the ascending segment of $S_I = f(S_E)$ (red nullcline). Following a similar argument as Wilson and Cowan [8], one notice that for the flow around a fixed point—an intersection between the nullclines—to have consistent rotation, the nullcline $g^{-1}(S_E)$ (blue) must have a greater slope than $f(S_E)$ (red nullcline). Qualitatively, one would expect oscillation to be induced by increasing w_{EI}, which twists $g(S_I)$ (blue nullcline) counterclockwise. This expectation is confirmed by the numerical results in Figure 3a-d: oscillation emerges for sufficiently large w_{EI} for fixed points on the ascending branch of $S_I = f(S_E)$ (Figure 4a-d).

Quantitatively, we consider the derivative of the two nullclines at a respective representative point. First, we extend the results in equation S17-S18 to the second nullcline $S_E = g(S_I)$ (blue):

$$S_I^* = \frac{1}{d_I \tau_I^{-1} \gamma_I^{-1} + 1} \tag{S20}$$

$$h_I := \left. \frac{\mathrm{d}\, H_I^{-1}(u(S_I))}{\mathrm{d}\, S_I} \right|_{S_I = S_I^*} = \frac{2(1 + d_I^{-1} \tau_I \gamma_I)^2}{a_I \tau_I \gamma_I}. \tag{S21}$$

For parameters used in the present study, $h_I \approx 0.4$. We have the slope of the two nullclines at their respective representative points,

$$f'(S_E^*) = \frac{w_{EE} - h_E}{w_{IE}} \tag{S22}$$

$$g'(S_I^*) = \frac{w_{II} + h_I}{w_{EI}}, \tag{S23}$$

and we need

$$\frac{1}{g'(S_I^*)} > f'(S_E^*) \tag{S24}$$

$$\Rightarrow \frac{w_{EI}}{w_{II} + h_I} > \frac{w_{EE} - h_E}{w_{IE}}$$

$$\Rightarrow w_{EI} > \frac{(w_{EE} - h_E)(w_{II} + h_I)}{w_{IE}}. \tag{S25}$$

With balanced inhibitory feedback $w_{IE} = w_{EE}$, we have

$$w_{EI} > (1 - h_E/w_{EE})(w_{II} + h_I). \tag{S26}$$

For very large w_{EE}, one simply need

$$w_{EI} > w_{II} + h_I. \tag{S27}$$

Given the present parameter choices, we need $w_{EI} > 0.45$ to induce oscillation for some level of input I_E and I_I. This is in line with the numerical results in Figure 3. For $h_E > 0$, as assumed here, lowering w_{EE} also lowers the threshold for oscillation.

Linear stability analysis. In addition to the presence of oscillation, one would also want to know if such oscillation is sustainable or damped. Here we extend the above analysis by linearizing the system near a specific fixed point. A fixed point is where the two nullclines (equations S9-S10) intersect. Conveniently, we let them intersect at their respective representative points $(S_E^*, f(S_E^*))$ and $(g(S_I^*), S_I^*)$ (see equation S17 and equation S20),

$$S_E^* = g(S_I^*) \tag{S28}$$

$$f(S_E^*) = S_I^*. \tag{S29}$$

41

The two equations can be satisfied by the appropriate choice of I_E and I_I. The fixed point of our choice (S_E^*, S_I^*) inherits a couple of properties from the above analysis, which we shall soon see. First, we define

$$\frac{\mathrm{d}\,S_E}{\mathrm{d}\,t} = F(S_E, S_I) := -\frac{S_E}{\tau_E} + (1 - S_E)\gamma_E\,H_E(w_{EE}S_E - w_{IE}S_I + I_E) \quad \text{(S30)}$$

$$\frac{\mathrm{d}\,S_I}{\mathrm{d}\,t} = G(S_E, S_I) := -\frac{S_I}{\tau_I} + (1 - S_I)\gamma_I\,H_I(w_{EI}S_E - w_{II}S_I + I_I). \quad \text{(S31)}$$

At the fixed points, we have from equation S30

$$H_E(w_{EE}S_E^* - w_{IE}S_I^* + I_E) = \frac{S_E^*}{\tau_E\gamma_E(1 - S_E^*)} \quad \text{(S32)}$$

$$= \frac{1}{d_E} \quad \text{(by definition, c.f. equation S16)} \quad \text{(S33)}$$

which implies that

$$I_E = \frac{b_E}{a_E} - w_{EE}S_E^* + w_{IE}S_I^* \quad \text{(S34)}$$

and

$$H_E'(w_{EE}S_E^* - w_{IE}S_I^* + I_E) = \frac{a_E}{2} \quad \text{(per equation S15).} \quad \text{(S35)}$$

Similarly from equation S31, we have

$$H_I(w_{EI}S_E^* - w_{II}S_I^* + I_I) = \frac{S_I^*}{\tau_I\gamma_I(1 - S_I^*)} = \frac{1}{d_I} \quad \text{(S36)}$$

$$I_I = \frac{b_I}{a_I} - w_{EI}S_E^* + w_{II}S_I^* \quad \text{(S37)}$$

$$H_I'(w_{EI}S_E^* - w_{II}S_I^* + I_I) = \frac{a_I}{2}. \quad \text{(S38)}$$

Now we are take the partial derivatives of F and G at (S_E^*, S_I^*),

$$\left.\frac{\partial F}{\partial S_E}\right|_{(S_E^*, S_I^*)} = -\frac{1}{\tau_E} - \gamma_E H_E(w_{EE}S_E^* - w_{IE}S_I^* + I_E)$$

$$+ (1 - S_E^*)\gamma_E w_{EE}H_E'(w_{EE}S_E^* - w_{IE}S_I^* + I_E)$$

$$= -\frac{1}{\tau_E} - \frac{\gamma_E}{d_E} + w_{EE}\gamma_E a_E(1 - S_E^*)/2 \quad \text{(S39)}$$

$$\left.\frac{\partial F}{\partial S_I}\right|_{(S_E^*, S_I^*)} = -(1 - S_I^*)w_{IE}\gamma_E H_E'(w_{EE}S_E^* - w_{IE}S_I^* + I_E)$$

$$= -w_{IE}\gamma_E a_E(1 - S_I^*)/2 \quad \text{(S40)}$$

$$\left.\frac{\partial G}{\partial S_E}\right|_{(S_E^*, S_I^*)} = (1 - S_I^*)w_{EI}\gamma_I H_I'(w_{EI}S_E^* - w_{II}S_I^* + I_I)$$

$$= w_{EI}\gamma_I a_I(1 - S_I^*)/2 \quad \text{(S41)}$$

$$\left.\frac{\partial G}{\partial S_I}\right|_{(S_E^*, S_I^*)} = -\frac{1}{\tau_I} - \gamma_I H_I(w_{EI}S_E^* - w_{II}S_I^* + I_I)$$

$$- (1 - S_I)w_{II}\gamma_I H_I'(w_{EI}S_E^* - w_{II}S_I^* + I_I)$$

$$= -\frac{1}{\tau_I} - \frac{\gamma_I}{d_I} - w_{II}\gamma_I a_I(1 - S_I^*)/2. \quad \text{(S42)}$$

42

For simplicity, let parameters

$$\alpha_p := \frac{1}{\tau_p} + \frac{\gamma_p}{d_p} \tag{S43}$$

$$\beta_p := \gamma_p a_p (1 - S_p^*)/2 \tag{S44}$$

$$= \frac{\gamma_p a_p d_p}{2(d_p + \gamma_p \tau_p)} \tag{S45}$$

for $p \in \{E, I\}$. Note that by definition, both α_p and β_p are positive. Given parameters used in the present study, we have $\alpha_E \approx 14$, $\alpha_I \approx 111$, $\beta_E \approx 71$, and $\beta_I \approx 276$.

We write the Jacobian matrix as

$$\mathbf{J} = \begin{pmatrix} -\alpha_E + \beta_E w_{EE} & -\beta_E w_{IE} \\ \beta_I w_{EI} & -\alpha_I - \beta_I w_{II} \end{pmatrix}. \tag{S46}$$

The eigenvalues of the Jacobian are

$$\lambda_{1,2} = \frac{\operatorname{tr}\mathbf{J} \pm \sqrt{\operatorname{tr}^2 \mathbf{J} - 4\det\mathbf{J}}}{2} \tag{S47}$$

where

$$\operatorname{tr}\mathbf{J} = -\alpha_E - \alpha_I + \beta_E w_{EE} - \beta_I w_{II} \tag{S48}$$

$$\det\mathbf{J} = \alpha_E \alpha_I + \alpha_E \beta_I w_{II} - \alpha_I \beta_E w_{EE} + \beta_I \beta_E (w_{IE} w_{EI} - w_{EE} w_{II}). \tag{S49}$$

Assuming that the system is already oscillatory near the fixed point, i.e. $\operatorname{tr}^2 \mathbf{J} < 4\det\mathbf{J}$, to have sustained oscillation (limit cycle), we need

$$\operatorname{tr}\mathbf{J} > 0$$
$$\Rightarrow w_{EE} > (\alpha_E + \alpha_I + \beta_I w_{II})/\beta_E. \tag{S50}$$

Given the parameters used in the present study, the emergence of limit cycles requires $w_{EE} > 2$. Correspondingly in the numerical results (Figure 3), equation S50 provides an estimate of the lower bound of the Hopf bifurcation (gray dashed line). Note that stronger inhibitory-to-inhibitory connection w_{II} increases the minimal w_{EE} required to induce sustained oscillation. Overall, these analyses show that sustained oscillation requires both strong self-excitation and a sufficiently active inhibitory population.

In summary, we have shown analytically how structural connectivity w_{EE} and w_{EI} critically shape the dynamics—in this very low-dimensional parameter space, the system can easily switch between qualitatively different behavior. In particular, excitatory-to-inhibitory connectivity w_{EI} controls the emergence of oscillation; excitatory-to-excitatory connectivity w_{EE} controls both the emergence of multistability and sustained oscillation. The qualitative description of the system only depends on the gross geometric form of the Wilson-Cowan model, but the exact boundaries between regimes depend on the specific transfer function and the associated biophysical constraints.

S8   Analysis of the global model

Now we take a look at the deterministic version of the global model,

$$\frac{\mathrm{d}\,S_E^{(i)}}{\mathrm{d}\,t} = -\frac{S_E^{(i)}}{\tau_E} + (1 - S_E^{(i)})\gamma_E H_E \left(w_{EE}^{(i)} S_E^{(i)} - w_{IE}^{(i)} S_I^{(i)} + I_G^{(i)}(\vec{S}_E) \right) \tag{S51}$$

$$\frac{\mathrm{d}\,S_I^{(i)}}{\mathrm{d}\,t} = -\frac{S_I^{(i)}}{\tau_I} + (1 - S_I^{(i)})\gamma_I H_I \left(w_{EI}^{(i)} S_E^{(i)} - w_{II}^{(i)} S_I^{(i)} + I_I \right) \tag{S52}$$

43

where

$$I_G^{(i)}(\vec{S}_E) = G \sum_{\substack{j=1 \\ j \neq i}}^{N} C_{ij} S_E^{(j)}. \tag{S53}$$

In this case, the nullclines are hyper-surfaces,

$$w_{IE}^{(i)} S_I^{(i)} = f^{(i)}\left(\vec{S}_E\right) := w_{EE}^{(i)} S_E^{(i)} - H_E^{-1}\left(\frac{S_E^{(i)}}{\tau_E \gamma_E (1 - S_E^{(i)})}\right) + G \sum_{j \neq i} C_{ij} S_E^{(j)} \tag{S54}$$

$$w_{EI}^{(i)} S_E^{(i)} = g^{(i)}\left(S_I^{(i)}\right) := w_{II}^{(i)} S_I^{(i)} + H_I^{-1}\left(\frac{S_I^{(i)}}{\tau_I \gamma_I (1 - S_I^{(i)})}\right) - I_I. \tag{S55}$$

From equation S54 one can see that the local effect of global coupling is simply tilting the nullcline $S_I^{(i)} = f^{(i)}\left(\vec{S}_E\right)/w_{IE}^{(i)}$ upwards with respect to $S_E^{(j)}$.

The tilting of the nullcline $S_I^{(i)} = f^{(i)}\left(\vec{S}_E\right)/w_{IE}^{(i)}$ impact its number of intersections with $S_E^{(i)} = g^{(i)}\left(S_I^{(i)}\right)/w_{EI}^{(i)}$ in each level set of $G \sum_{j \neq i} C_{ij} S_E^{(j)}$. The number of intersections consequently constrains the number of stable states. A precise characterization of intersections is beyond the scope of the present work. Nevertheless, we hope to provide a few insights about the global geometry below.

Multistability. Following a similar argument as for the local model, we first show that, without global interaction (i.e. $G = 0$), the system cannot be multistable, if w_{EE} is sufficiently small such that $f^{(i)}(\vec{S}_E)$ monotonically decreases with $S_E^{(i)}$ for all i. As shown above, the monotonicity condition implies that each local node by itself is not multistable.

Proof. Assume there are at least two distinct fixed points of the system: $\vec{S}^*$ and $\vec{S}^{**}$, where $\vec{S} = (\vec{S}_E, \vec{S}_I)$ and $\vec{S}_p = (S_p^{(1)}, \cdots S_p^{(i)}, \cdots S_p^{(N)})$ for $p \in \{E, I\}$. Since they are distinct points, there exists an $0 < i \leqslant N$ such that $S_E^{*(i)} \neq S_E^{**(i)}$ ($S_I^{*(i)} \neq S_I^{**(i)}$ implies $S_E^{*(i)} \neq S_E^{**(i)}$ due to the monotonicity of g). Without loss of generality, we let $S_E^{*(i)} < S_E^{**(i)}$.

Since we know that $g^{-1\,(i)}(w_{EI}^{(i)} S_E^{(i)})$ is always a monotonically increasing function, we have

$$g^{-1\,(i)}(w_{EI}^{(i)} S_E^{*(i)}) < g^{-1\,(i)}(w_{EI}^{(i)} S_E^{**(i)}) \tag{S56}$$

$$\Rightarrow S_I^{*(i)} < S_I^{**(i)}, \tag{S57}$$

which also implies that

$$f^{(i)}\left(\vec{S}_E^*\right) < f^{(i)}\left(\vec{S}_E^{**}\right) \tag{S58}$$

by definition of the nullcline $S_I^{(i)} = f^{(i)}\left(\vec{S}_E\right)/w_{IE}^{(i)}$, for any choice of G and C_{ij}.

Now if $f^{(i)}(\vec{S}_E)$ is monotonically decreasing with respect to $S_E^{(i)}$, we know that at least for $G = 0$,

$$f^{(i)}\left(\vec{S}_E^*\right) > f^{(i)}\left(\vec{S}_E^{**}\right), \tag{S59}$$

which leads to a contradiction. Thus, if the system has multiple fixed points, $f^{(i)}(\vec{S}_E)$ cannot be monotonically decreasing with respect to $S_E^{(i)}$ for all i when $G = 0$. $\square$

However, given a sufficiently large global coupling, especially for $G > 1$, multistability becomes possible.

44

Proof. Following the above proof, the assumption $S_E^{*(i)} < S_E^{**(i)}$ leads us to equation S58, or $\Delta_G < 0$, where

$$\Delta_G := f_G^{(i)}\left(\vec{S}_E^*\right) - f_G^{(i)}\left(\vec{S}_E^{**}\right) \tag{S60}$$

for any global coupling $G \geqslant 0$.

On the other hand, for the special case of $G = 0$, we can plug equation S54 into the definition S60 and have

$$\Delta_0 = f_{G=0}^{(i)}\left(\vec{S}_E^*\right) - f_{G=0}^{(i)}\left(\vec{S}_E^{**}\right) = w_{IE}^{(i)}\left(S_I^{*(i)} - S_I^{**(i)}\right) \tag{S61}$$

$$= f_{G=0}^{(i)}\left(S_E^{*(i)}\right) - f_{G=0}^{(i)}\left(S_E^{**(i)}\right) > 0, \tag{S62}$$

by our assumption that $f_G^{(i)}(\vec{S}_E)$ is a monotonically decreasing function with respect to $S_E^{(i)}$. Since by definition, the coordinates of each fixed point is bounded between 0 and 1, we have

$$0 < \Delta_0 \leqslant w_{IE}^{(i)}. \tag{S63}$$

In the case of $G = 0$, this leads to a contradiction $\Delta_G > 0$, as we have already shown above.

Now we consider what happens when $G > 0$. Again, by plugging equation S54 into the definition S60, we have

$$\Delta_G = \Delta_0 + G\sum_{j \neq i} C_{ij} S_E^{*(j)} - G\sum_{j \neq i} C_{ij} S_E^{**(j)}$$

$$= \Delta_0 + G\sum_{j \neq i} C_{ij}(S_E^{*(j)} - S_E^{**(j)}). \tag{S64}$$

We need a bound on the second term in equation S64. Since $G > 0$ and $C_{ij} \geqslant 0$,

$$\left| G\sum_{j \neq i} C_{ij}(S_E^{*(j)} - S_E^{**(j)}) \right| \leqslant G\sum_{j \neq i} C_{ij}\left|(S_E^{*(j)} - S_E^{**(j)})\right|$$

$$\leqslant G\sum_{j \neq i} C_{ij} \qquad (\text{since } 0 \leqslant S_E^{(j)} \leqslant 1)$$

$$\leqslant G \qquad (\text{by equation 7}).$$

This gives us

$$\Delta_0 - G \leqslant \Delta_G \leqslant \Delta_0 + G. \tag{S65}$$

Thus, contradiction with equation S58 is inevitable if $G < \Delta_0$. On the other hand, by equation S63, we know that for $G > \Delta_0$, there exists some $\vec{S}_E^*$ and $\vec{S}_E^{**}$ for some global network C_{ij} such that $\Delta_G < 0$ consistent with equation S58. Thus it is possible for the global model to be multistable if $G > \Delta_0$, especially if $G > w_{IE}^{(i)}$, or $G > w_{EE}^{(i)}$ given matched inhibitory feedback $w_{EE} = w_{IE}$. This does not mean, however, that the system has to be multistable, due to the dependency on C_{ij}. $\square$

To summarize, the above analyses suggest that a collection of brain regions that have no independent memory capacity (i.e. multistability) can *acquire* memory capacity when connected to each other in a global network, given sufficient global coupling. We further support this claim with numerical analysis (Figure S6). We refer to this kind of memory as *synergistic* memory—it is an emergent property that the parts themselves do not possess.
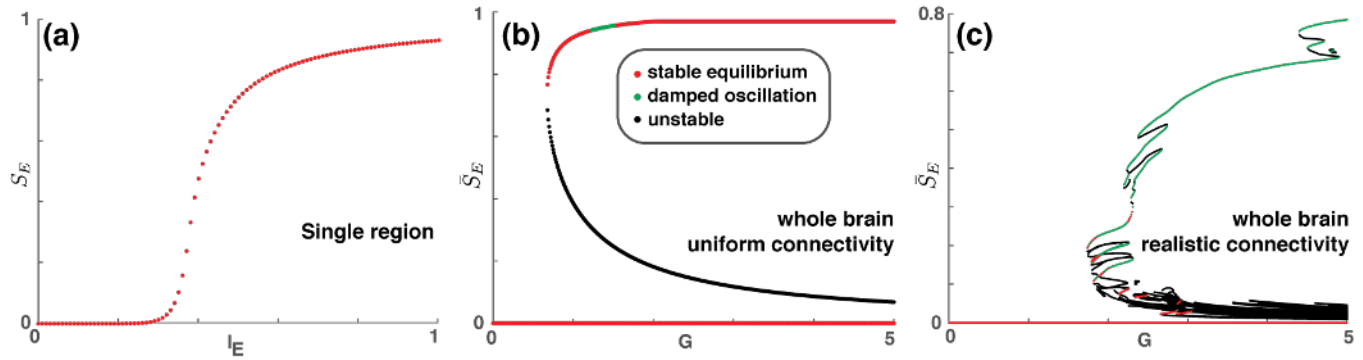
45

Figure S6: **Synergistic memory between monostable nodes**. Three bifurcation diagrams are shown for local parameters $w_{EE} = 0.1$ and $w_{EI} = 0.35$. They correspond to Figure 7a, d, g but with a lower w_{EE} such that each local node by itself is monostable for any level of input (a). While each local node is completely monostable (no memory capacity), once there is sufficient global coupling G between them, the whole brain acquires memory capacity (b, c) that cannot be attributed to the parts alone—synergistic memory. Nevertheless, the size of the global memory capacity is still fundamentally constrained by the complexity of the local node (42 attractor branches in (c), very small compare to Figure 7g, h, i). See text for further discussion.

What we have not addressed in the above analyses is to what extent the global system is multistable—what is the number of stable states, or the size of the memory capacity—and what are the contributions from local self-excitation and global network connectivity. An analytical approach to this problem is difficult; thus, it is mainly addressed numerically (c.f. Figure S6 and Figure 7). Nevertheless, we provide an intuitive argument below as to how local and global connectivity affects the relevant geometrical properties of the dynamical system.

Local origin of geometrical complexity. At an intuitive level, the number of intersections between these hypersurfaces (equation S54-S55) is likely to increase with the number of folds of each surface. In the present case, the folding of hypersurfaces entails the temporary reversal of the sign of its partial derivative along a certain direction. Observe equation S54 and see that global coupling cannot create any folding of the surfaces. Thus, the geometrical complexity of the nullclines purely depends on the local properties of each node, in particular, the folding effect of self-excitation $w_{EE}^{(i)}$.

The effect of global coupling. Without global coupling ($G = 0$), the number of fixed points of the global model is simply

$$n = \prod_{i=1}^{N} n_0^{(i)} \leqslant \left(\max_i n_0^{(i)} \right)^N \tag{S66}$$

where $n_0^{(i)}$ is the number of fixed points for each corresponding local model when $I_E = 0$. Introducing global coupling ($G \neq 0$) tilts each surface (equation S54) in a way dependent on the structure connectivity C_{ij}. This may remove or introduce new intersections between the surfaces without changing the geometrical complexity of these surfaces. Thus, global coupling allows system-level multistability to be created synergistically, given appropriate structural connectivity C_{ij}.

In summary, local and global coupling produce different geometrical effects on the system and jointly affect the number of possible stable states.

46

References 1100

1. Buxton, R. B., Wong, E. C. & Frank, L. R. Dynamics of blood flow and 1101 oxygenation changes during brain activation: The balloon model. *Magnetic* 1102 *Resonance in Medicine* **39,** 855–864 (1998). 1103

2. Mandeville, J. B. *et al.* Evidence of a Cerebrovascular Postarteriole Windkessel 1104 with Delayed Compliance. *Journal of Cerebral Blood Flow & Metabolism* **19,** 1105 679–689 (1998). 1106

3. Friston, K., Mechelli, A., Turner, R. & Price, C. Nonlinear responses in fMRI: 1107 the Balloon model, Volterra kernels, and other hemodynamics. *NeuroImage* 1108 **12** (2000). 1109

4. Friston, K., Harrison, L. & Penny, W. Dynamic causal modelling. *NeuroImage* 1110 **19,** 1273–1302 (2003). 1111

5. Welch, P. The use of fast Fourier transform for the estimation of power spectra: 1112 A method based on time averaging over short, modified periodograms. *IEEE* 1113 *Transactions on Audio and Electroacoustics* **15,** 70–73 (1967). 1114

6. Van Essen, D. C. *et al.* The WU-Minn Human Connectome Project: An 1115 overview. *NeuroImage* **80,** 62–79 (2013). 1116

7. Wong, K.-F. & Wang, X.-J. A recurrent network mechanism of time integration 1117 in perceptual decisions. *Journal of Neuroscience* **26,** 1314–1328 (2006). 1118

8. Wilson, H. R. & Cowan, J. D. Excitatory and inhibitory interactions in 1119 localized populations of model neurons. *Biophysical Journal* **12,** 1–24 (1972). 1120

47